Correlation between Electrocatalytic Activity and Impedance Shape: A Theoretical Analysis

Jun Huang[1,2,*]

[1]*Institute of Energy and Climate Research, IEK-13: Theory and Computation of Energy Materials, Forschungszentrum Jülich GmbH, 52425 Jülich, Germany*

[2]*Theory of Electrocatalytic Interfaces, Faculty of Georesources and Materials Engineering, RWTH Aachen University, 52062 Aachen, Germany*

Though electrochemical impedance spectroscopy (EIS) has been widely used in mechanistic investigations of electrocatalytic reactions, the correlation between the shape of an EIS diagram and the electrocatalytic activity is largely unclear; the complexity of electrocatalytic reactions in terms of reaction mechanisms and influencing factors casts an air of pessimism over the existence and, if it exists, the stability of such a correlation. Nevertheless, understanding the correlation can help select reaction mechanisms and electrical circuit models in data analysis, use the EIS shape as a descriptor of electrocatalytic activity, and detect side reactions if the measured shapes deviate from the theoretical prediction based on the main reaction. Herein, the problem is tackled by a systematic mathematical analysis of firstly single-adsorbate reactions and then more complicated reactions involving multiple adsorbates. A complete regime diagram of all possible EIS shapes of single-adsorbate reactions is provided, navigating the subsequent analysis in the multidimensional parametric space. For single-adsorbate reactions involving two steps with identical transfer coefficients of 0.5 in the absence of lateral adsorbate interactions, several rigorous remarks on the EIS shape are made. Unfortunately, many of them require modifications when different transfer coefficients and lateral interactions are considered. Nevertheless, several trends in EIS shapes are robust against complexities of reaction mechanisms and variations in reaction parameters, which also receive experimental evidence collected from the literature. The theoretical analysis presented here may trigger interest in finding a correlation between the impedance shape and the electrocatalytic activity across a wide range of reactions.

I. INTRODUCTION

To avert dire consequences of climate change, our society requires a radical transformation in the way of supplying, transforming, and using energy. A key discipline underlying this transformation is electrocatalysis, which is concerned with how catalysts accelerate the speed of electrochemical reactions by facilitating making and breaking of chemical bonds. Many crucial technologies currently need precious electrocatalysts. For example, the oxygen reduction reaction in polymer electrolyte fuel cells is catalyzed by platinum-based materials. A major goal of electrocatalysis research is the rational design and screening of cheap and stable electrocatalysts. Relevant methods are founded on simple correlations between performance metrics and intrinsic properties of electrocatalysts; such intrinsic properties are termed descriptors of activity [1–3].

In the past, many descriptors have been proposed, ranging from characteristic parameters of electronic structure of electrocatalysts, e.g., *d*-band center of transition metals [1,4], to characteristic parameters of the chemical bond formed between electrocatalysts and reaction intermediates, e.g., binding energy of adsorbed hydroxyl in oxygen reduction (evolution) reactions [5,6]. In the latter case, the relationship between the electrocatalytic activity and the binding energy resembles a volcano shape, as depicted in Fig. 1 [7,8]. The volcano plot of activity indicates that the optimal electrocatalyst shall bind reaction intermediates neither too strongly nor too weakly, which is essentially Sabatier's principle of catalysis.

Let us digress for a moment from the catalytic view on electrocatalysis and introduce the electrochemical view.
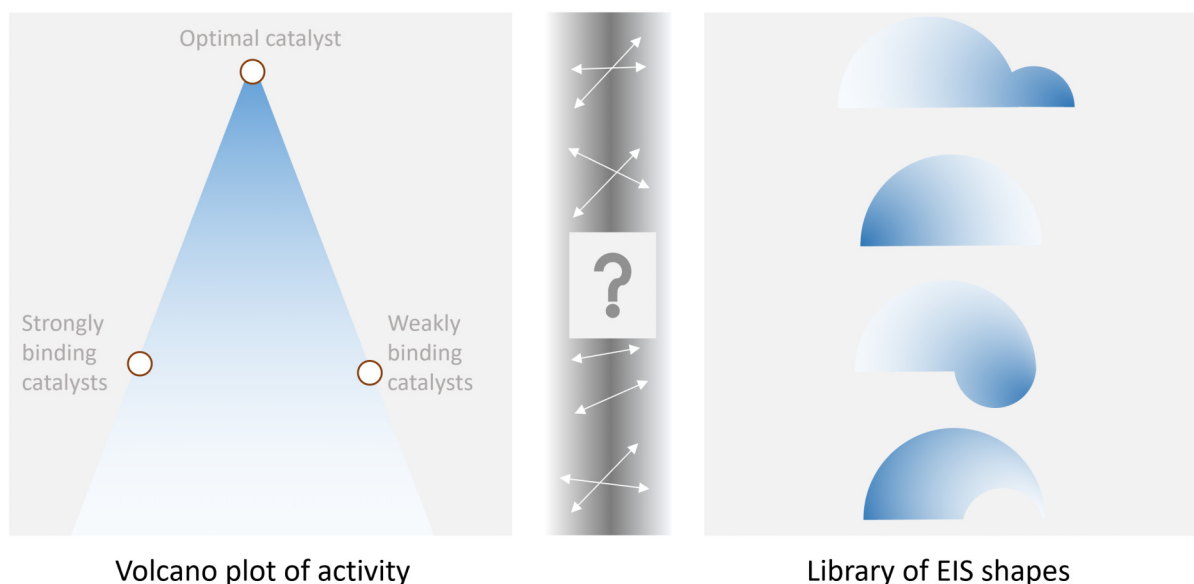
---

*[*]ju.huang@fz-juelich.de

FIG. 1. This study is motivated by a general question: is there any correspondence between (left) the volcano plot of activity and (right) shapes of the electrochemical impedance spectroscopy in the Nyquist plot, with Z' being the real part and Z'' the imaginary part?

For several decades, electrochemists have been trying to decipher the mechanism of electrocatalytic reactions by applying various voltage-current techniques, among which electrochemical impedance spectroscopy (EIS) is often used, as it allows the reaction to be dissected over a wide frequency range, spanning more than 10 orders of magnitude [9–31]. A comprehensive review of EIS studies on electrocatalytic reactions is beyond the scope of this paper; see a recent review, Ref. [32]. Below, we just mention a few earlier works in chronological order. Discussions on the relationship between the present work and works in the literature are scattered throughout this paper.

Dolin and Ershler measured the rate of hydrogen adsorption at platinum using EIS in 1940 and developed a mathematical model for EIS of a single chemisorption process [33]. Gerischer and Mehl studied EIS of hydrogen evolution reactions in 1955 and developed an EIS model for this multistep electrocatalytic reaction with the kinetics of elementary steps described by the Tafel equation [11]. The Gerischer-Mehl approach was applied to anodic dissolution of iron with FeOH as the intermediate by Epelboin and Keddam in 1970 [12], generalized to any reactions with one intermediate by Armstrong and Henderson in 1972 [13], and extended to Butler-Volmer kinetics by Harrington and Conway in 1987 [16]. It was shown that the EIS diagrams could have different shapes, as depicted in Fig. 1. In the 1980s, Diard, Le Gorrec, and Montella studied how the shape of EIS diagrams of a Volmer-Heyrovsky reaction was related to the kinetic parameters of the reaction [15,17,19]. The analysis method was recently applied to other reactions [34,35]. Harrington formulated a general

theory for EIS of multistep electrocatalytic reactions in the 1990s [20–23], and recently simplified his theory based on the rate-determining step approximation [29,31]. Gabrielli [36] and Lasia [37] published excellent tutorials on the EIS of electrocatalytic reactions.

The catalytic and electrochemical lines have been proceeding more or less independently, and the link between them is less explored. Specifically, the correlation between the EIS shape and the activity of the catalyst is largely ambiguous. This situation might be ascribed to the prevailing pessimism that EIS shapes of electrocatalytic reactions are unfortunately unstable against variations in the reaction mechanism and parameters, as illustrated in many studies [15,17,19,36,37]. Hence, questions like "do electrocatalysts located in the strongly, weakly, and optimally adsorbing sections of the volcano plot have different EIS shapes?" remain largely unanswered. The primary motivation of this work is thus to bridge the catalytic and electrochemical lines of electrocatalysis research, and to bring optimism to the search for some stable correlations between EIS shapes and electrocatalytic activity.

In the following, we start by deriving the EIS of single-adsorbate reactions, which is not new but serves the purpose of acquainting readers from the catalysis field with the language of impedance modeling. Afterwards, we present a complete regime diagram of all mathematically possible EIS shapes of single-adsorbate reactions, which provides a global map for the analysis of EIS shapes in the multidimensional parametric space. With kinetic parameters described by Butler-Volmer equations, the model can be readily used to generate volcano plots of activity and a

library of EIS diagrams. A rigorous mathematical analysis on single-adsorbate reactions with identical transfer coefficients of 0.5 for both elementary steps and free of lateral adsorbate interactions lead to several remarks regarding the EIS shapes corroborated with rigorous mathematical proofs. When different transfer coefficients and lateral interactions are considered, most of these remarks fail miserably and only a few are found to remain valid. The analysis is then generalized to arbitrary reactions with diffusion of reactants and products. The generalized model is then demystified with a rudimentary example and simplified further using the concept of the rate-determining term. Before the conclusion section, experimental evidence for a few findings is also collected from the literature. It is stressed from the outset that the present analysis takes the *forward* path, namely, analyzing EIS plots of a kinetic model, while the *backward* path, namely, interrogating the kinetic model from the EIS plots, is not taken.

II. FARADAIC IMPEDANCE OF SINGLE-ADSORBATE REACTIONS

Let us start with the following two-step reaction with a single-adsorbed intermediate:

$$R + {}^* + n_a e \leftrightarrow I_{ad}, \qquad (a)$$

$$I_{ad} + n_b e \leftrightarrow P + {}^*, \qquad (b)$$
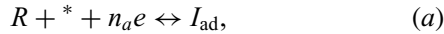
where R is the reactant, I_{ad} is the adsorbed intermediate, P is the product, and n_a and n_b are the numbers of electrons transferred in each step. Since each elementary step can transfer one electron at most, n_a and n_b can adopt three values, 0 (chemical reaction), 1 (reduction in the forward direction), and -1 (oxidation in the forward direction). It will be made clear shortly that the EIS derived for this two-step mechanism is general for any single-adsorbate reactions.

We denote the net reaction rates (equivalently, the turnover frequency) of steps (a) and (b) as v_a and v_b with a unit of s^{-1}, which are functions of the coverage of I_{ad}, θ, and the electrode potential E:

$$v_a = v_a(\theta, E), \ v_b = v_b(\theta, E). \qquad (1)$$

The rate of change for θ is given by

$$\frac{d\theta}{dt} = v_a - v_b. \qquad (2)$$

The charge-transfer current density, i_{ct}, which is positive for oxidation, is written as

$$i_{ct} = -Q(n_a v_a + n_b v_b), \qquad (3)$$

where Q corresponds to the charge density of a full monolayer of I_{ad} with a unit of C m^{-2}.

In impedance measurements, the system is brought away from the stationary state while remaining in the linear response regime. In the potentiostatic mode, a voltage stimulus, denoted $E(t) = \bar{E} + \tilde{E}e^{j\omega t}$, is applied, where stationary quantities are denoted with an overbar, and the perturbations with an overtilde. Ensured by the linearity condition, variations in any system variable X follows, $X(t) = \bar{X} + \tilde{X}e^{j\omega t}$. Specifically, the reaction rates read

$$v_i(t) = \bar{v}_i + \tilde{v}_i e^{j\omega t}, \qquad (4)$$

with total differential relations

$$\tilde{v}_i = \left(\frac{\partial v_i}{\partial \theta}\right)_{\bar{E}} \tilde{\theta} + \left(\frac{\partial v_i}{\partial E}\right)_{\bar{\theta}} \tilde{E}. \qquad (5)$$

Therefore, Eq. (2) is transformed into

$$0 = \bar{v}_a - \bar{v}_b, \qquad (6)$$

$$j\omega\tilde{\theta} = \tilde{v}_a - \tilde{v}_b, \qquad (7)$$

where Eq. (6) corresponds to the stationary condition, and the second the linear perturbation.

Combining Eqs. (5) and (7), we link $\tilde{\theta}$ and $\tilde{E}$ as

$$\tilde{\theta} = \frac{\Delta_E}{j\omega - \Delta_\theta} \tilde{E}, \qquad (8)$$

with

$$\Delta_E = \left(\frac{\partial v_a}{\partial E}\right)_{\bar{\theta}} - \left(\frac{\partial v_b}{\partial E}\right)_{\bar{\theta}},$$

and

$$\Delta_\theta = \left(\frac{\partial v_a}{\partial \theta}\right)_{\bar{E}} - \left(\frac{\partial v_b}{\partial \theta}\right)_{\bar{E}},$$

being two partial derivative differences.

We can then obtain $\tilde{i}_{ct}$ as a function of $\tilde{E}$,

$$\tilde{i}_{ct} = -\left(\frac{\Sigma_\theta \Delta_E}{j\omega - \Delta_\theta} + \Sigma_E\right)\tilde{E}, \qquad (9)$$

by substituting Eqs. (5) and (8) into Eq. (3), with

$$\Sigma_\theta = Q\left(n_a\left(\frac{\partial v_a}{\partial \theta}\right)_{\bar{E}} + n_b\left(\frac{\partial v_b}{\partial \theta}\right)_{\bar{E}}\right),$$

and

$$\Sigma_E = Q\left(n_a\left(\frac{\partial v_a}{\partial E}\right)_{\bar{\theta}} + n_b\left(\frac{\partial v_b}{\partial E}\right)_{\bar{\theta}}\right),$$

being two partial derivative sums.

The measured current density, $\tilde{i}_{\text{tot}}$, is the sum of $\tilde{i}_{\text{ct}}$ and a double-layer charging part,

$$\tilde{i}_{\text{dl}} = j\,\omega C_{\text{dl}}\tilde{E}, \tag{10}$$

with the differential double-layer capacitance, C_{dl}.

The impedance defined as $Z = \tilde{E}/\tilde{i}_{\text{tot}}$ is obtained as

$$Z = \frac{1}{j\,\omega C_{\text{dl}} - ((\Sigma_\theta \Delta_E / j\,\omega - \Delta_\theta) + \Sigma_E)}, \tag{11}$$

which can be reformulated as

$$Z = \frac{1}{j\,\omega C_{\text{eff}}(\omega) + (R_{\text{eff}}(\omega))^{-1}}, \tag{12}$$

which has the form of the Randles-Ershler model, but now with an effective frequency-dependent capacitance,

$$C_{\text{eff}}(\omega) = C_{\text{dl}} + \frac{\Sigma_\theta \Delta_E}{\omega^2 + \Delta_\theta^2}, \tag{13}$$

and an effective frequency-dependent resistance,

$$R_{\text{eff}}(\omega) = \left(-\Sigma_E + \frac{\Sigma_\theta \Delta_E \Delta_\theta}{\omega^2 + \Delta_\theta^2} \right)^{-1}. \tag{14}$$

C_{eff} is asymptotic to C_{dl} when $\omega \to \infty$, and to $C_0 = C_{\text{dl}} + (\Sigma_\theta \Delta_E / \Delta_\theta^2)$ when $\omega \to 0$. R_{eff} is asymptotic to $(-\Sigma_E)^{-1}$ when $\omega \to \infty$, and to $R_0 = (-\Sigma_E + (\Sigma_\theta \Delta_E / \Delta_\theta))^{-1}$ when $\omega \to 0$. It is the frequency dispersion of C_{eff} and R_{eff} that leads to different shapes of EIS diagrams, otherwise the EIS diagram has a single semicircle.

Equation (11) is essentially the same result as that derived by Armstrong and Henderson in 1972 [13], later by Harrington and Conway [16], Cao [18], and Lasia [38]. Harrington and Conway used another set of variables that are related to the present set of variables as $A = -\Sigma_E$, $B = -\Sigma_\theta \Delta_E$, and $C = -\Delta_\theta$, and manipulated Eq. (11) into four different forms, corresponding to four different equivalent electrical circuits [16]. Caveats of associating the structure of an electric circuit with a reaction mechanism, that is, taking the backward path, were discussed there. It is important to note that the impedance form expressed in Eq. (11) is not limited to the two-step sequential reaction mechanism. In fact, Eq. (11) is universal for any reaction involving a single-adsorbed intermediate, as revealed by Harrington and Conway [16], Cao [18], and Lasia [38]. To illustrate this universality, we follow Cao [18] and reformulate Eqs. (2) and (3) as

$$\frac{d\theta}{dt} = g(E, \theta), \tag{15}$$

$$i_{\text{ct}} = f(E, \theta), \tag{16}$$

where f and g are two general functions. By the same procedure of perturbation analysis, we obtain the impedance

in the form of Eq. (11) with

$$\Sigma_E = -\left(\frac{\partial i_{\text{ct}}}{\partial E}\right)_{\bar{E}}, \quad \Delta_\theta = \left(\frac{\partial g}{\partial \theta}\right)_{\bar{E}}, \quad \Delta_E = \left(\frac{\partial g}{\partial E}\right)_{\bar{E}}, \quad \Sigma_\theta$$

$$= -\left(\frac{\partial i_{\text{ct}}}{\partial \theta}\right)_{\bar{E}}. \tag{17}$$

The hydrogen evolution reaction is the most studied example of single-adsorbate reactions [11,37–39]. The impedance of the Volmer-Heyrovsky-Tafel mechanism was derived by Gerischer and Mehl using Tafel kinetics [11], which was extended by Harrington and Conway using Butler-Volmer kinetics [16], and by Lasia further considering lateral interactions [38]. Simplified expressions and electric circuits for different scenarios have been given by Harrington [29,31] and Lasia [37,38]. Bisquert and Guerrero recently used this single-adsorbate reaction as an example of a general theory of chemical inductors [40,41].

III. REGIME DIAGRAM OF IMPEDANCE SHAPES

The Nyquist plot of Z, namely, the real part (Z') versus negative of the imaginary part $(-Z'')$ at a series of frequencies, is determined by five parameters: C_{dl}, Σ_θ, Δ_E, Σ_E, and Δ_θ. The last four are composite parameters contingent on the detailed expression of charge-transfer theory and depend characteristically on the electrode potential. Herein, we use them as parameters and defer a mechanistic analysis to later sections. The purpose here is to enumerate all mathematically possible impedance shapes.

Epelboin and Keddam discussed when an inductive low-frequency loop occurred in the Nyquist plot for the iron dissolution reaction [12]. Cao analyzed systematically EIS shapes for a general electrode process depending on E and another state variable, X, e.g., the surface coverage of the intermediate [18]. Considering a Volmer-Heyrovsky mechanism, Diard *et al.* presented a phase diagram for EIS shapes with respect to two reaction parameters [19]. Inspired by and as a continuation of these studies, we present below a regime diagram of EIS shapes for single-adsorbate reactions, which is originally five dimensional for we have five parameters C_{dl}, Σ_θ, Δ_E, Σ_E, and Δ_θ. Since $\Delta_E \Sigma_\theta$ always appear together in the model, Δ_E and Σ_θ are not varied separately in the following analysis; instead, $\Delta_E \Sigma_\theta$ is taken as a single parameter. Therefore, our analysis has the same degree of freedom as in the analysis of Harrington and Conway, where $A = -\Sigma_E$, $B = -\Sigma_\theta \Delta_E$, and $C = -\Delta_\theta$ are used [16].

In Fig. 2, we set Δ_θ as the x axis, and the product of Σ_θ and Δ_E, denoted $\Pi = \Delta_E \Sigma_\theta$, as the y axis. In addition, we introduce a straight line, $y_1 = \Sigma_E \Delta_\theta$, with the slope Σ_E always being negative. and a parabolic curve described as $y_2 = -C_{\text{dl}} \Delta_\theta^2$, which is related to the sign of $C_{\text{eff}}(\omega \to 0)$.

The two axes, the straight line, and the parabolic curve thus divide the full space into nine subregions. In the following analysis, we frequently refer to Eq. (13) for C_{eff} and Eq. (14) for R_{eff}.

In region 1 of $(\Sigma_\theta \Delta_E > 0, \, \Delta_\theta > 0)$, provided that $C_{dl} > 0$ and $\Sigma_E < 0$,

$$C_{eff} = C_{dl} + \frac{\Sigma_\theta \Delta_E}{\omega^2 + \Delta_\theta^2},$$

and

$$R_{eff} = \left(-\Sigma_E + \frac{\Sigma_\theta \Delta_E \Delta_\theta}{\omega^2 + \Delta_\theta^2}\right)^{-1},$$

are always positive. Hence, the Nyquist plot is in the first quadrant, see Fig. 2(1) for an example. The thumblike shape is caused by the fact that R_{eff} decreases when ω decreases (denoted $\omega \downarrow$ in the plots).

In region 2a of $(\Sigma_\theta \Delta_E > \Delta_\theta \Sigma_E > 0, \, \Delta_\theta < 0)$, $C_{eff} = C_{dl} + (\Sigma_\theta \Delta_E / \omega^2 + \Delta_\theta^2)$ is always positive, while R_{eff} transits from $(-\Sigma_E)^{-1} > 0$, when $\omega \to \infty$, to

$$\left(-\Sigma_E + \frac{\Sigma_\theta \Delta_E}{\Delta_\theta}\right)^{-1} < 0,$$

when ω decreases towards zero ($\omega \to 0$ for short). This means a thumblike shape starting from the first quadrant and ending in the second quadrant; see Fig. 2(2a). In region 2b of $(0 < \Sigma_\theta \Delta_E < \Delta_\theta \Sigma_E, \, \Delta_\theta < 0)$, C_{eff} is always positive, and R_{eff} increases when $\omega \to 0$, resulting in two semicircles in the first quadrant; see Fig. 2(2b).

In region 3a of

$$(-C_{dl}\Delta_\theta^2 < \Sigma_\theta \Delta_E < 0, \Delta_\theta < 0),$$

$$C_{eff} = C_{dl} + \frac{\Sigma_\theta \Delta_E}{\omega^2 + \Delta_\theta^2},$$

and

$$R_{eff} = \left(-\Sigma_E + \frac{\Sigma_\theta \Delta_E \Delta_\theta}{\omega^2 + \Delta_\theta^2}\right)^{-1},$$

are always positive, and R_{eff} decreases from $(-\Sigma_E)^{-1} > 0$, when $\omega \to \infty$, to

$$\left(-\Sigma_E + \frac{\Sigma_\theta \Delta_E}{\Delta_\theta}\right)^{-1} > 0,$$

when $\omega \to 0$, resulting in a gradually suppressed semicircle in the first quadrant; see Fig. 2(3a). In region 3b of $(\Sigma_\theta \Delta_E < -C_{dl}\Delta_\theta^2, \, \Delta_\theta < 0)$, C_{eff} transits from C_{dl} when $\omega \to \infty$ to $(C_{dl} + (\Sigma_\theta \Delta_E / \Delta_\theta^2)) < 0$ when $\omega \to 0$, while R_{eff} decreases but remains positive as $\omega \to 0$, resulting in a semicircle in the first quadrant followed by an inverse

semicircle (also termed an inductive loop) in the fourth quadrant; see Fig. 2(3b).

In region 4a of $\Sigma_\theta \Delta_E < \min(-C_{dl}\Delta_\theta^2, \Sigma_E \Delta_\theta)$, $\Delta_\theta > 0$, C_{eff} decreases from $C_{dl} > 0$ when $\omega \to \infty$ to $(C_{dl} + (\Sigma_\theta \Delta_E / \Delta_\theta^2)) < 0$ when $\omega \to 0$, and R_{eff} decreases from $(-\Sigma_E)^{-1} > 0$ when $\omega \to \infty$ to $(-\Sigma_E + (\Sigma_\theta \Delta_E / \Delta_\theta))^{-1} < 0$ when $\omega \to 0$. Since both C_{eff} and R_{eff} transit from positive to negative when ω decreases, we obtain a semicircle in the first quadrant followed by an inverse semicircle spanning over the third and fourth quadrants; see Fig. 2(4a). In region 4b of $\Sigma_E \Delta_\theta < \Sigma_\theta \Delta_E < -C_{dl}\Delta_\theta^2, \, \Delta_\theta > 0$, C_{eff} transits from positive to negative while R_{eff} increases when ω decreases, resulting in a semicircle in the first quadrant followed by an inverse semicircle in the fourth quadrant extending further along the x axis; see Fig. 2(4b). In region 4c of $\max(-C_{dl}\Delta_\theta^2, \Sigma_E \Delta_\theta) < \Sigma_\theta \Delta_E < 0, \Delta_\theta > 0$, both C_{eff} and R_{eff} increase when ω decreases, resulting in a larger higher-frequency and a smaller lower-frequency semicircle in the first quadrant; see Fig. 2(4c). In region 4d of $-C_{dl}\Delta_\theta^2 < \Sigma_\theta \Delta_E < \Sigma_E \Delta_\theta, \, \Delta_\theta > 0$, C_{eff} increases while R_{eff} transits from positive to negative when ω decreases, resulting in a bulb shape spanning the first and second quadrants; see Fig. 2(4d).

Not all regions shown in Fig. 2 are permissible in real situations. As shown in the next section, we have $\Delta_\theta < 0$ for most cases, except in the presence of strongly attractive interactions between adsorbates in Fig. 12, and $\Sigma_E < 0$ for all cases, while the signs of Σ_θ and Δ_E are contingent on kinetic parameters and electrode potential. Given that $\Delta_\theta < 0$, Cao maintained that the condition of occurrence of an inductive arc on the impedance plane was $\Sigma_\theta \Delta_E < 0$ [18]. From the above analysis, it is clear that this conclusion is not rigorously true, because an inductive arc is absent in regime 3a though $\Sigma_\theta \Delta_E < 0$. Cao's conclusion should be weakened to "the condition of occurrence of an inductive arc on the impedance plane is $\Sigma_\theta \Delta_E < -C_{dl}\Delta_\theta^2$." In line with our analysis, Lasia recently pointed out that "the condition $B > 0$ ($B = -\Sigma_\theta \Delta_E$ in the present formalism) is not sufficient as there must be correct combination of other kinetic parameters and double-layer capacitance to be able to observe it" [38].

IV. CORRELATION BETWEEN IMPEDANCE SHAPE AND ACTIVITY FOR SINGLE-ADSORBATE REACTIONS

Having obtained a complete understanding of the possible shapes of the EIS, we proceed to correlate the EIS shape and the electrocatalytic activity. To this end, we need to specify $k_i^\pm$ as functions of the electrode potential and the surface coverage of the adsorbate.

Specifically, we consider herein a two-electron reduction reaction with $n_a = n_b = 1$ in steps (a) and (b). The net
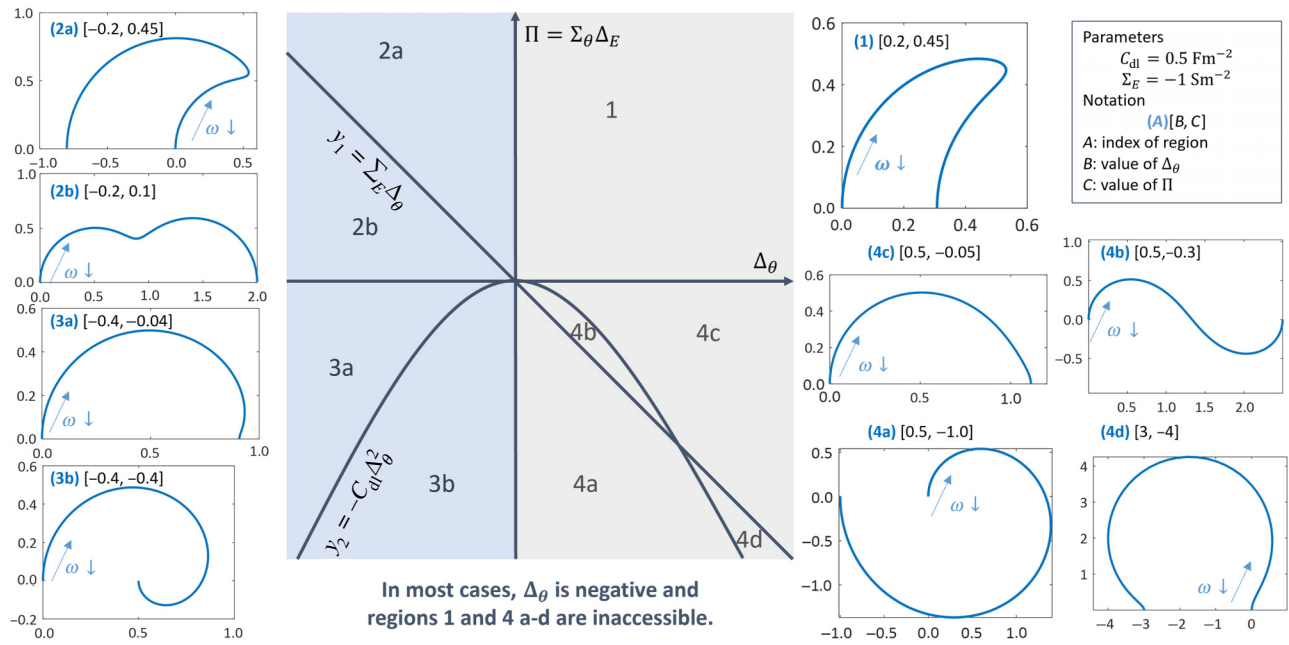
FIG. 2. Regime diagram of Nyquist plots of EIS of single-adsorbate reactions. The x axis is the real part of impedance with units of Ω m^2 and the y axis is the negative of the imaginary part of impedance with units of Ω m^2. Δ_θ is set as the x axis, and the product of Σ_θ and Δ_E is the y axis. Straight line, $y_1 = \Sigma_E \Delta_\theta$; a parabolic curve, $y_2 = -C_{dl}\Delta_\theta^2$; and the two axes divide the phase space into nine regions. Legend in each subplot is composed of one index and two numbers, which are explained in the notation box. We have $C_{dl} > 0$ and $\Sigma_E < 0$. In addition, unless for the case of very strong attractive lateral interactions between adsorbates, $\Delta_\theta < 0$ is usually met, in which cases regions 1 and 4(a)–(d) are inaccessible.

reaction rates are written as

$$v_a = k_a^+(\theta_{\max} - \theta) - k_a^-\theta, \quad v_b = k_b^+\theta - k_b^-(\theta_{\max} - \theta),$$
(18)

where rate "constants" are given by

$$k_a^+ = k_0 \exp(-\beta(\Delta G_a^\ddagger + \alpha_a e(E - E_a + \gamma(\theta - \theta_a)))),$$

$$k_a^- = k_0 \exp(-\beta(\Delta G_a^\ddagger - (1-\alpha_a)e(E - E_a + \gamma(\theta - \theta_a)))),$$

$$k_b^+ = k_0 \exp(-\beta(\Delta G_b^\ddagger + \alpha_b e(E - E_b - \gamma(\theta - \theta_b)))),$$

$$k_b^- = k_0 \exp(-\beta(\Delta G_b^\ddagger - (1-\alpha_b)e(E - E_b - \gamma(\theta - \theta_b)))),$$

with k_0 being the preexponential factor; $\Delta G_a^\ddagger$ and $\Delta G_b^\ddagger$ are the activation barriers of steps (a) and (b) under equilibrium, respectively; α_a and α_b are the transfer coefficients; E_a and E_b are the equilibrium potentials; θ_a and θ_b are the adsorbate coverages at the equilibrium potentials of steps (a) and (b), respectively; γ is the lateral interaction coefficient with a unit of V; $\beta = 1/k_B T$ is the inverse temperature; e is the magnitude of the elementary charge; and $\theta_{\max}$ is the maximal surface coverage. We note that lateral interactions, though ubiquitous in electrocatalysis and vital to electrocatalytic activity, were not considered in most previous EIS works; one exception can be found in a recent comprehensive study by Lasia [38].

We rescale E by taking $(E_a + E_b)/2$ as the reference value and define the difference in the activation barrier, $\Delta B = \Delta G_a^\ddagger - \Delta G_b^\ddagger$, and the difference in the equilibrium potential, $\Delta E = (E_a - E_b)/2$. We note that ΔB is not related to the variable B introduced in the work of Harrington and Conway [16]. As the adsorbed intermediate is formed in step (a) and consumed in step (b), ΔE is exactly the negative of the adsorption free energy of the adsorbed intermediate ΔG up to a constant e, namely, $\Delta E = -\Delta G/e$. ΔG and ΔB have units of eV in this paper. A more positive (negative) ΔE corresponds to stronger (weaker) adsorption. Below, we use ΔG as the descriptor of activity, namely, the x axis in the volcano plot. Now we reformulate the rate constants as

$$k_a^+ = A_0 \exp\left(-\alpha_a \beta e\left(E + \frac{\Delta G}{e} + \gamma(\theta - \theta_a)\right)\right),$$

$$k_a^- = A_0 \exp\left((1-\alpha_a)\beta e\left(E + \frac{\Delta G}{e} + \gamma(\theta - \theta_a)\right)\right),$$

$$k_b^+ = A_0 \exp\left(\beta\Delta B - \alpha_b \beta e\left(E - \frac{\Delta G}{e} - \gamma(\theta - \theta_b)\right)\right),$$

$$k_b^- = A_0 \exp\left(\beta\Delta B + (1-\alpha_b)\beta e\left(E - \frac{\Delta G}{e} - \gamma(\theta - \theta_b)\right)\right),$$
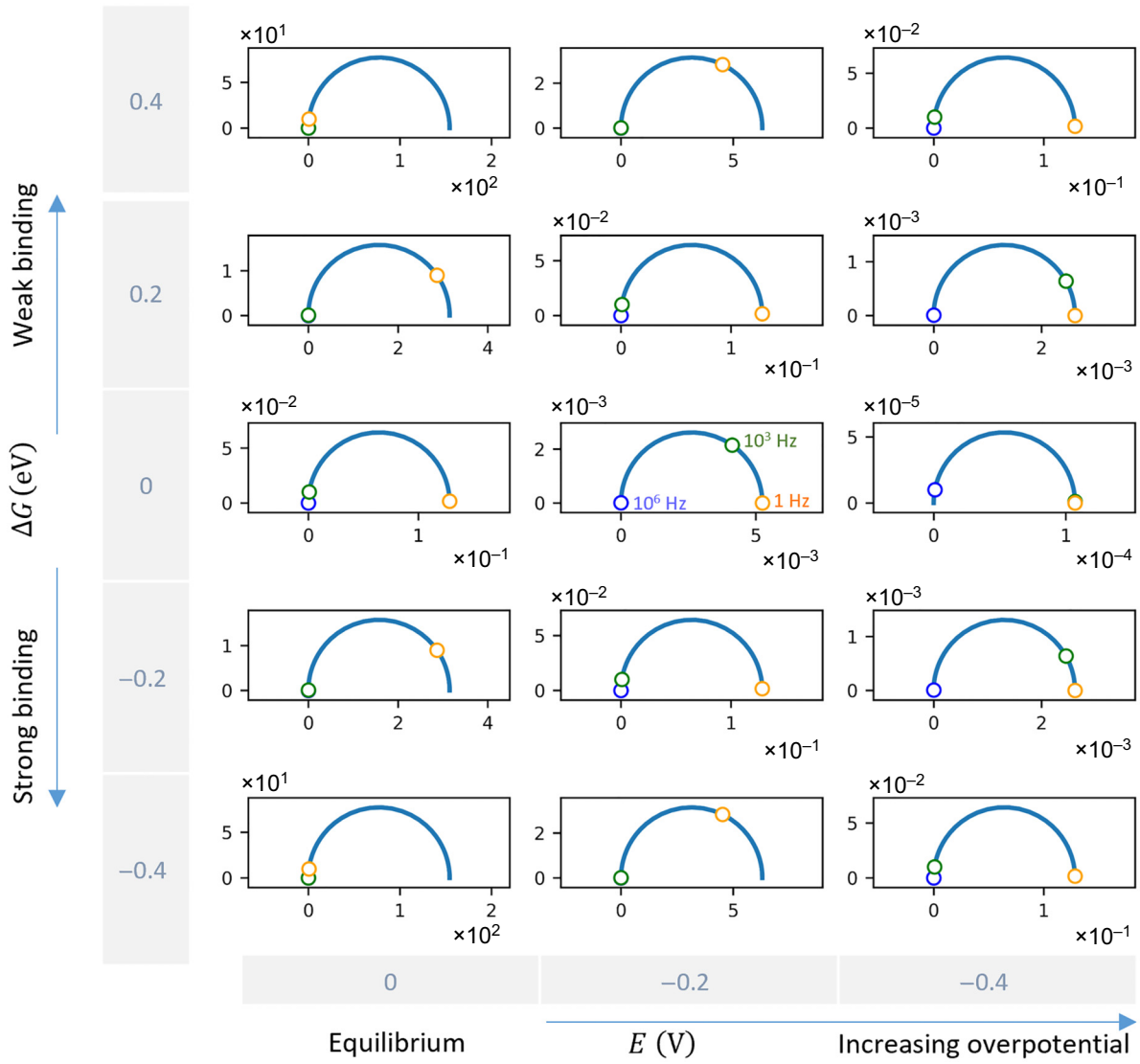
with $A_0 = k_0 \exp(-\beta\Delta G_a^a)$.

FIG. 3. EIS shapes at equal barriers ($\Delta B = 0$ eV). Nyquist plots of EIS at three electrode potentials and five binding energies (ΔG) are shown with parameters, $\alpha_a = \alpha_b = 0.5$, $\gamma = 0$, $\theta_{max} = 1$, $A_0 = 0.1$ s^{-1}, $C_{dl} = 0.1$ F m^{-2}, $Q = 2$ C m^{-2}, $\Delta B = 0$ eV. Horizontal and vertical axes of the EIS plot represent the real and negative imaginary parts of the impedance (Ωm^2), respectively. In some plots, the scientific notation of the impedance value is used in the horizontal and vertical axes.

According to the steady state expressed in Eq. (6), we solve Eq. (18) and obtain

$$\bar{\theta} = \theta_{max} \frac{k_a^+ + k_b^-}{k_a^+ + k_a^- + k_b^+ + k_b^-}. \tag{19}$$

θ_a and θ_b are obtained from Eq. (19) at E_a and E_b, respectively. When step (a) is at equilibrium, namely, when $E = -\Delta G/e$, we have $k_a^+ = k_a^- = A_0$, and $k_b^+ = A_0 \exp(\beta \Delta B - \alpha_b \beta(-2\Delta G - e\gamma(\theta_a - \theta_b)))$, $k_b^- = A_0 \exp(\beta \Delta B + (1 - \alpha_b)\beta(-2\Delta G - e\gamma(\theta_a - \theta_b)))$, and

$$\theta_a = \theta_{max} \frac{1 + e^{\beta \Delta B + (1-\alpha_b)\beta(-2\Delta G - e\gamma(\theta_a - \theta_b))}}{2 + e^{\beta \Delta B - \alpha_b \beta(-2\Delta G - e\gamma(\theta_a - \theta_b))} + e^{\beta \Delta B + (1-\alpha_b)\beta(-2\Delta G - e\gamma(\theta_a - \theta_b))}}. \tag{20}$$

Similarly, when step (b) is at equilibrium, we have

$$\theta_b = \theta_{max} \frac{1 + e^{-\beta \Delta B - \alpha_a \beta(2\Delta G - e\gamma(\theta_a - \theta_b))}}{2 + e^{-\beta \Delta B - \alpha_a \beta(2\Delta G - e\gamma(\theta_a - \theta_b))} + e^{-\beta \Delta B + (1-\alpha_a)\beta(2\Delta G - e\gamma(\theta_a - \theta_b))}}. \tag{21}$$
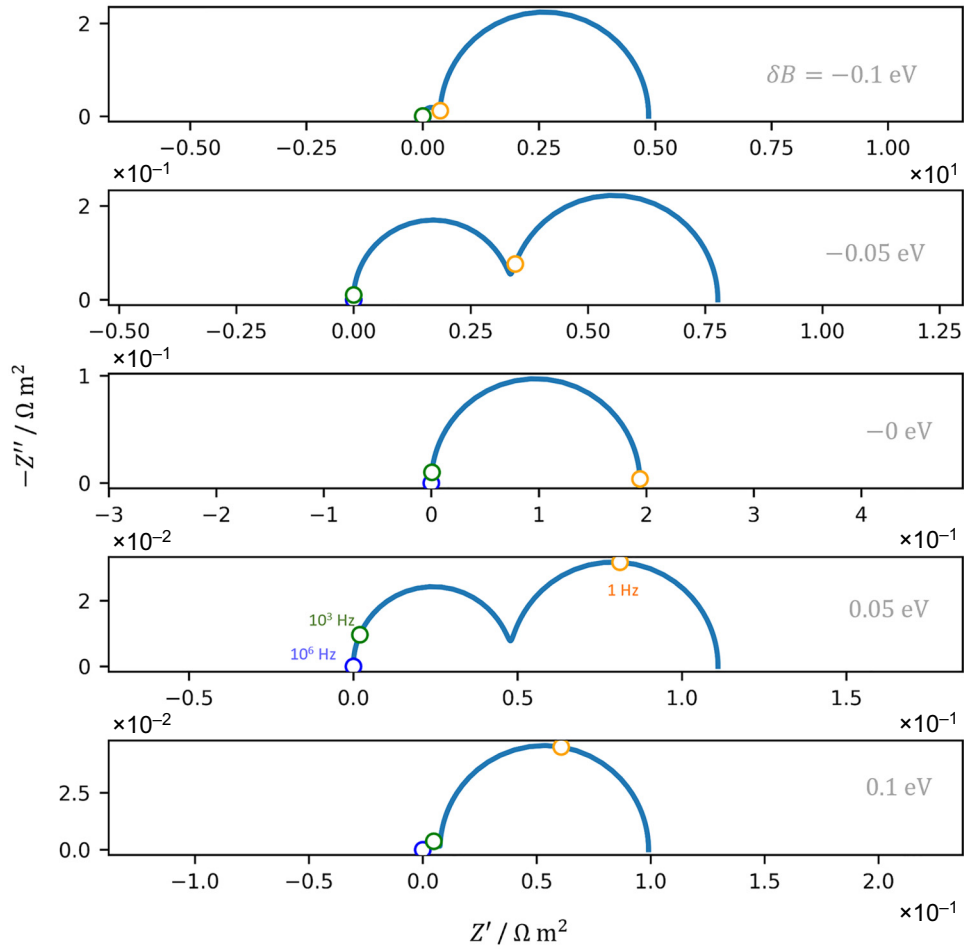
FIG. 4. EIS shapes at equilibrium potential ($E = 0$ V). Nyquist plots of EIS at equilibrium potential at five barrier differences (ΔB) with $\alpha_a = \alpha_b = 0.5$, $\gamma = 0$, $\theta_{max} = 1$, $A_0 = 0.1$ s^{-1}, $C_{dl} = 0.1$ F m^{-2}, $Q = 2$ C m^{-2}, $\Delta G = -0.05$ eV are shown.

In cases of lateral interactions between adsorbates, θ_a and θ_b should be solved self-consistently from Eqs. (20) and (21).

At steady state, the partial derivatives are calculated as

$$\left(\frac{\partial v_a}{\partial E}\right)_{\bar{\theta}} = -\beta e(\alpha_a k_a^+(\theta_{max} - \bar{\theta}) + (1 - \alpha_a)k_a^-\bar{\theta}), \quad (22)$$

$$\left(\frac{\partial v_b}{\partial E}\right)_{\bar{\theta}} = -\beta e(\alpha_b k_b^+\bar{\theta} + (1 - \alpha_b)k_b^-(\theta_{max} - \bar{\theta})), \quad (23)$$

$$\left(\frac{\partial v_a}{\partial \theta}\right)_{\bar{E}} = -k_a^+ - k_a^- + \gamma\left(\frac{\partial v_a}{\partial E}\right)_{\bar{\theta}}, \quad (24)$$

$$\left(\frac{\partial v_b}{\partial \theta}\right)_{\bar{E}} = k_b^+ + k_b^- - \gamma\left(\frac{\partial v_b}{\partial E}\right)_{\bar{\theta}}. \quad (25)$$

Substituting these partial derivatives into Σ_θ, Δ_E, Σ_E, and Δ_θ, respectively, we obtain

$$\Sigma_\theta = Q(k_b^+ + k_b^- - k_a^+ - k_a^-) + \gamma\Delta_E, \quad (26)$$

$$\Delta_\theta = -(k_a^+ + k_a^- + k_b^+ + k_b^-) + \frac{\gamma\Sigma_E}{Q}, \quad (27)$$

$$\Sigma_E = -\beta eQ\frac{(k_a^+k_a^- + k_b^+k_b^-) + k_a^+k_b^+(\alpha_a + \alpha_b) + k_a^-k_b^-(2 - (\alpha_a + \alpha_b))}{k_a^+ + k_a^- + k_b^+ + k_b^-}, \quad (28)$$

$$\Delta_E = -\beta e\frac{(k_a^+k_a^- - k_b^+k_b^-) + (k_a^+k_b^+ - k_a^-k_b^-)(\alpha_a - \alpha_b)}{k_a^+ + k_a^- + k_b^+ + k_b^-}. \quad (29)$$

As k_a^+, k_a^-, k_b^+, and k_b^- are positive and $0 < \alpha_a + \alpha_b < 2$, we know $\Sigma_E < 0$ for all cases, $\Delta_\theta < 0$ for all cases with $\gamma > 0$, and the signs of Σ_θ and Δ_E vary from case to case. As a result, only four regions, 2a, 2b, 3a, and 3b, in Fig. 2 are permissible for the ordinary case of $\gamma > 0$. Given any set of A_0, ΔB, and ΔG, we can calculate Σ_θ, Δ_E, Σ_E, Δ_θ, the reaction rate (i.e., catalytic activity), and the impedance response at any electrode potential.

We consider firstly the ideal and most-studied case of $\alpha_a = \alpha_b = 0.5$ and $\gamma = 0$, then consider different transfer coefficients $\alpha_a \neq \alpha_b$ and finally nonzero lateral interactions $\gamma \neq 0$. For the sake of visual neatness, we use dimensionless variables defined as $\tilde{E} = \beta e E$, $\Delta\tilde{G} = \beta \Delta G$, $\Delta\tilde{B} = \beta \Delta B$. The analysis is structured in the following manner. A remark on the EIS shape is presented, followed by a mathematical proof and numerical examples.

A. Ideal case of $\alpha_a = \alpha_b = 0.5$ and $\gamma = 0$

The rate constants are now written as $k_a^+ = A_0 e^{-(\tilde{E}+\Delta\tilde{G})/2}$, $k_a^- = A_0 e^{(\tilde{E}+\Delta\tilde{G})/2}$, $k_b^+ = A_0 e^{\Delta\tilde{B}-(\tilde{E}-\Delta\tilde{G})/2}$, $k_b^- = A_0 e^{\Delta\tilde{B}+(\tilde{E}-\Delta\tilde{G})/2}$, and the four key parameters in the impedance expression are

$$\Sigma_\theta = 2QA_0 \left[e^{\Delta\tilde{B}} \cosh\frac{\tilde{E}-\Delta\tilde{G}}{2} - \cosh\frac{\tilde{E}+\Delta\tilde{G}}{2} \right], \tag{30}$$

$$\Delta_\theta = -2A_0 \left[e^{\Delta\tilde{B}} \cosh\frac{\tilde{E}-\Delta\tilde{G}}{2} + \cosh\frac{\tilde{E}+\Delta\tilde{G}}{2} \right], \tag{31}$$

$$\Sigma_E = -\frac{Q\beta e A_0}{2} \frac{\left(e^{-(\tilde{E}+\Delta\tilde{G})/2} + e^{\Delta\tilde{B}} e^{(\tilde{E}-\Delta\tilde{G})/2} \right) \left(e^{(\tilde{E}+\Delta\tilde{G})/2} + e^{\Delta\tilde{B}} e^{-(\tilde{E}-\Delta\tilde{G})/2} \right)}{e^{\Delta\tilde{B}} \cosh(\tilde{E}-\Delta\tilde{G})/2 + \cosh(\tilde{E}+\Delta\tilde{G})/2}, \tag{32}$$

$$\Delta_E = \frac{\beta e A_0}{2} \frac{e^{2\Delta\tilde{B}} - 1}{e^{\Delta\tilde{B}} \cosh(\tilde{E}-\Delta\tilde{G})/2 + \cosh(\tilde{E}+\Delta\tilde{G})/2}. \tag{33}$$

Remark 1. Consider a two-step single-adsorbate electrochemical reaction with $\alpha_a = \alpha_b = 0.5$ and $\gamma = 0$. Its EIS has only one semicircle in the Nyquist plot, if the two steps have equal barriers, namely, $\Delta\tilde{B} = 0$.

Numerical examples are given in Fig. 3. With a set of parameters, $\alpha_a = \alpha_b = 0.5$, $\gamma = 0$, $A_0 = 0.1$ s^{-1}, $C_{dl} = 0.1$ F m^{-2}, $Q = 2$ C m^{-2}, $\Delta B = 0$ eV, the EIS plots show only one semicircle at different potentials and binding energies. This remark is further corroborated by a rigorous mathematical analysis. Given that $\Delta\tilde{B} = 0$, Eq. (33) gives $\Delta_E = 0$. Therefore, $C_{\text{eff}} = C_{dl} + (\Sigma_\theta \Delta_E / \omega^2 + \Delta_\theta^2) = C_{dl}$ and

$$R_{\text{eff}} = \left(-\Sigma_E + \frac{\Sigma_\theta \Delta_E \Delta_\theta}{\omega^2 + \Delta_\theta^2} \right)^{-1} = (-\Sigma_E)^{-1},$$

and the EIS only has one semicircle in the Nyquist plot.

Remark 2. Consider a two-step single-adsorbate electrochemical reaction with $\alpha_a = \alpha_b = 0.5$ and $\gamma = 0$. At

equilibrium potential, namely, $\tilde{E} = 0$, catalysts fall into region 2 in Fig. 2. The EIS shape is composed of two semicircles without an inductive loop.

In Fig. 4, we give five EIS plots at equilibrium potential with different values of ΔB. two semicircles are found in all cases other than $\Delta B = 0$ eV, which has been described in **Remark 1**. The relative sizes of the two semicircles differ more at larger ΔB, according to the following mathematical analysis. Given that $\tilde{E} = 0$, Eqs. (30)–(33) are reduced to

$$\Sigma_\theta = 2QA_0(e^{\Delta\tilde{B}} - 1)\cosh\frac{\Delta\tilde{G}}{2},$$

$$\Delta_\theta = -2A_0(e^{\Delta\tilde{B}} + 1)\cosh\frac{\Delta\tilde{G}}{2},$$

$$\Sigma_E = -\beta e Q \frac{(1 + e^{\Delta\tilde{B}})}{2\cosh(\Delta\tilde{G}/2)},$$

$$\Delta_E = \beta e \frac{e^{\Delta\tilde{B}} - 1}{\cosh(\Delta\tilde{G}/2)}.$$

Therefore,

$$\Sigma_\theta \Delta_E = 2\beta e Q A_0 (e^{\Delta\tilde{B}} - 1)^2 > 0,$$

$$\Delta_\theta \Sigma_E = 2\beta e Q A_0 (e^{\Delta\tilde{B}} + 1)^2,$$

and

$$\frac{\Sigma_\theta \Delta_E}{\Delta_\theta \Sigma_E} = \left(\tanh\left(\frac{\Delta\tilde{B}}{2}\right) \right)^2.$$

Therefore, all catalysts fall into region 2 in Fig. 2.

Remark 3. Consider a two-step single-adsorbate electrochemical reaction with $\alpha_a = \alpha_b = 0.5$ and $\gamma = 0$. Its EIS shape is dominated by a single semicircle at high overpotentials.

At very high overpotentials, $|\tilde{E}| \gg \max\{|\Delta\tilde{B}|, |\Delta\tilde{G}|\}$, an order analysis of Eqs. (30)–(33) gives

$$\left| \frac{\Sigma_\theta \Delta_E}{\Delta_\theta \Sigma_E} \right| \approx e^{-|\tilde{E}|} \approx 0.$$

This means that the low-frequency semicircle, be it capacitive or inductive, has a much smaller magnitude than the high-frequency one. Hence, the overall EIS shape visibly shows a single semicircle.

In Fig. 5, the volcano plots of activity and EIS plots are shown at different potentials and binding energies, with parameters $\alpha_a = \alpha_b = 0.5$, $\gamma = 0$, $A_0 = 0.1 \text{ s}^{-1}$, $C_{dl} = 0.1 \text{ F m}^{-2}$, $Q = 2 \text{ C m}^{-2}$, and $\Delta B = 0.06$ eV. The EIS plots at high overpotentials, say -0.4 V, show a single semicircle. The reaction rate, r (s^{-1}), firstly increases and then decreases with ΔG; see Fig. 5(a). When the electrode potential, E, becomes more negative, namely, the overpotential for this reductive reaction increases, r grows. The peak of the volcano is found not at the thermodynamic expectation, $\Delta G = 0$ eV. Instead, it is found at a negative ΔG, that is, a slightly strong binding catalyst since the adsorption step has a higher barrier than desorption. A more detailed analysis of the potential-dependent volcano peak is given in Ref. [42]. The EIS of the most active catalyst is displayed in Fig. 6 at the examined potentials. It consists of two semicircles at small overpotentials and one semicircle at large overpotentials. No inductive loop is observed.

Remark 4. Consider a two-step single-adsorbate electrochemical reaction with $\alpha_a = \alpha_b = 0.5$ and $\gamma = 0$. The thermodynamically optimal catalyst, namely, $\Delta\tilde{G} = 0$, falls into region 2 in Fig. 2. The EIS shape is composed of two semicircles without an inductive loop.

When $\Delta\tilde{G} = 0$, we rewrite Eqs. (30)–(33) as

$$\Sigma_\theta = 2QA_0 \left(e^{\Delta\tilde{B}} - 1 \right) \cosh\frac{\tilde{E}}{2}, \tag{34}$$

$$\Delta_\theta = -2A_0 \left(e^{\Delta\tilde{B}} + 1 \right) \cosh\frac{\tilde{E}}{2}, \tag{35}$$

$$\Sigma_E = -\frac{\beta e Q A_0}{2} \frac{1 + e^{\Delta\tilde{B}} \left(e^{\tilde{E}} + e^{-\tilde{E}} \right) + e^{2\Delta\tilde{B}}}{\left(e^{\Delta\tilde{B}} + 1 \right) \cosh(\tilde{E}/2)}, \tag{36}$$

$$\Delta_E = \frac{\beta e A_0}{2} \frac{e^{2\Delta\tilde{B}} - 1}{\left(e^{\Delta\tilde{B}} + 1 \right) \cosh\left(\tilde{E}/2\right)}. \tag{37}$$

Hence, $\Sigma_\theta \Delta_E > 0$ and the optimal catalyst fall into region 2 in Fig. 2, and no inductive loop is expected. Examples are given by the EIS plots in the middle line of Fig. 5(b). The EIS plots are composed of two semicircles of potential-dependent ratios in the first quadrant.

Remark 5. Consider a two-step single-adsorbate electrochemical reaction with $\alpha_a = \alpha_b = 0.5$ and $\gamma = 0$. Catalysts that adsorb the intermediate very weakly ($\Delta\tilde{G} \gg 0$) or very strongly ($\Delta\tilde{G} \ll 0$), namely, low-activity catalysts, possess only one semicircle. No inductive loop is expected.

When $\Delta\tilde{G} \gg 0$, we approximate Eqs. (30)–(33) as

$$\Sigma_\theta \approx 2QA_0 \left(e^{\Delta\tilde{B} - (\tilde{E}/2)} - e^{\tilde{E}/2} \right) e^{\Delta\tilde{G}/2}, \tag{38}$$

$$\Delta_\theta \approx -2A_0 \left(e^{\Delta\tilde{B} - (\tilde{E}/2)} + e^{\tilde{E}/2} \right) e^{\Delta\tilde{G}/2}, \tag{39}$$

$$\Sigma_E \approx -\frac{\beta e Q A_0}{2} \frac{1 + e^{\Delta\tilde{B}} \left(e^{\tilde{E}} + e^{-\tilde{E}} \right) + e^{2\Delta\tilde{B}}}{e^{\Delta\tilde{B} - (\tilde{E}/2)} + e^{\tilde{E}/2}} e^{-\Delta\tilde{G}/2}, \tag{40}$$

$$\Delta_E \approx \frac{\beta e A_0}{2} \frac{e^{2\Delta\tilde{B}} - 1}{e^{\Delta\tilde{B} - (\tilde{E}/2)} + e^{\tilde{E}/2}} e^{-\Delta\tilde{G}/2}. \tag{41}$$

Therefore, $|\Delta_\theta| \propto e^{\Delta\tilde{G}/2} \gg |\Sigma_E| \propto e^{-\Delta\tilde{G}/2}$. The characteristic frequency of the semicircle is $\omega_c = (1/C_{dl})|\Sigma_E|$. Hence, $|\Delta_\theta| \gg \omega_c$, and we can approximate the impedance in the frequency range near ω_c as

$$Z = \frac{1}{j\omega C_{dl} - ((\Sigma_\theta \Delta_E/j\omega - \Delta_\theta) + \Sigma_E)}$$

$$\approx \frac{1}{j\omega C_{dl} - (\Sigma_E - (\Sigma_\theta \Delta_E/\Delta_\theta))},$$

implying that we observe only one semicircle and there is no inductive loop, as illustrated by the EIS plots in the top line of Fig. 5(b).

When $\Delta\tilde{G} \ll 0$, following the same reasoning as for the case of $\Delta\tilde{G} \gg 0$, we know $|\Delta_\theta| \propto e^{-\Delta\tilde{G}/2} \gg |\Sigma_E| \propto e^{\Delta\tilde{G}/2}$. Therefore, the same conclusion also holds, as shown in the bottom line of Fig. 5(b). The EIS plots are composed of one semicircle in the first quadrant.
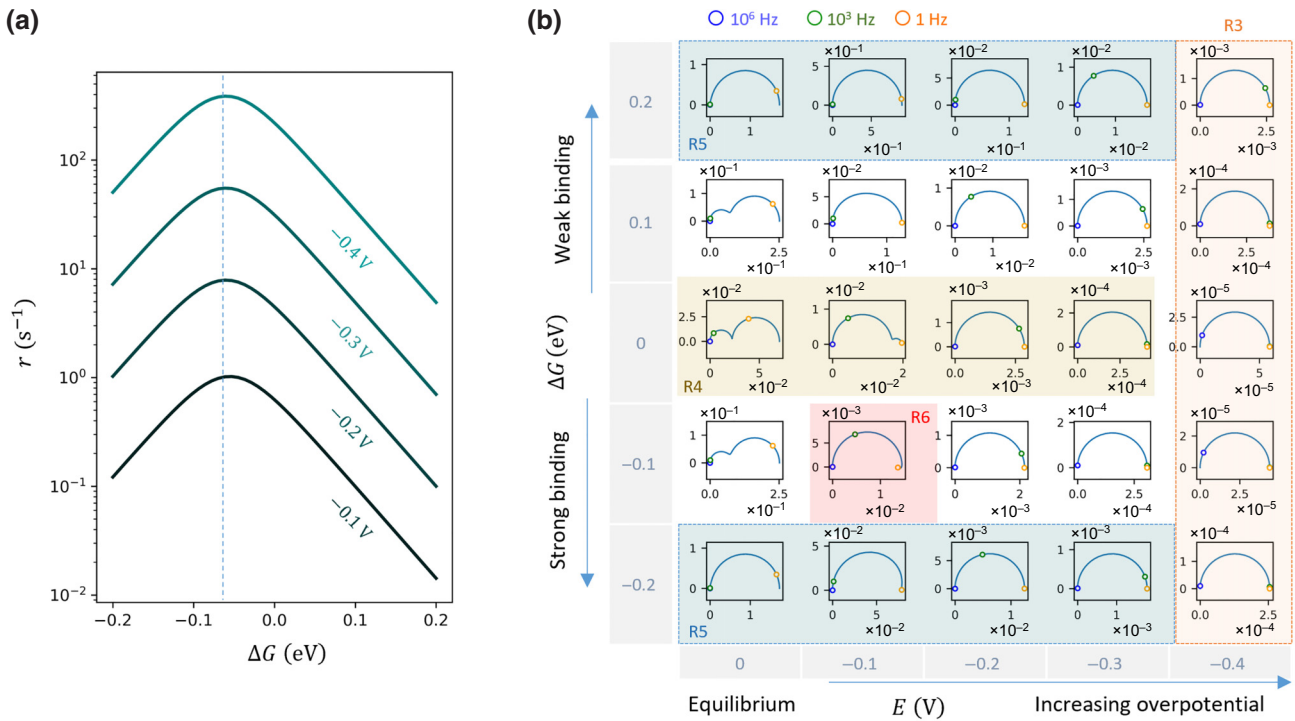
FIG. 5.   Correlation between EIS shapes and activity for single-adsorbate reactions. (a) Volcano plots of activity and (b) Nyquist plots of EIS at different electrode potentials and binding energies (ΔG) are obtained with parameters, $\alpha_a = \alpha_b = 0.5, \gamma = 0, \theta_{max} = 1, A_0 = 0.1 \ \text{s}^{-1}, C_{dl} = 0.1 \ \text{F m}^{-2}, Q = 2 \ \text{C m}^{-2}, \Delta B = 0.06 \ \text{eV}$. Horizontal and vertical axes of the EIS plot represent the real and negative imaginary parts of the impedance (Ωm^2), respectively. The PYTHON code for generating this figure is provided in the Supplemental Material [43]. Rn corresponds to Remark n.

Remark 6. Consider a two-step single-adsorbate electrochemical reaction with $\alpha_a = \alpha_b = 0.5$ and $\gamma = 0$. Necessary conditions to observe an inductive loop in the low-frequency range include (1) thermodynamically nonoptimal ($\Delta\tilde{G} \neq 0$) but not too far from the optimal catalyst in the volcano plot; (2) low-moderate overpotentials; and (3) nonzero barrier difference between adsorption and desorption step, more specifically, the adsorption barrier is higher (lower) than the desorption barrier at slightly overbinding (underbinding) catalysts.

Condition (1) is derived by combining **Remarks 4** and **6**. **Remark 4** stipulates that the thermodynamically optimal catalyst cannot have an inductive loop. **Remark 6** implies that the adsorption energy should not be too positive nor negative, otherwise only one semicircle is expected. Condition (2) is derived from **Remarks 2** and **3**. The first part of condition (3), nonzero barrier difference between adsorption and desorption step, is derived from **Remark 1**. Furthermore, since $\Sigma_\theta \Delta_E < 0$ is a necessary condition for the inductive loop, Eqs. (46)–(49) indicate that $\Sigma_\theta \Delta_E < 0$ is possible only when $\Delta\tilde{B} < 0$ for the case of $\Delta\tilde{G} \gg 0$ and $\Delta\tilde{B} > 0$ for the case of $\Delta\tilde{G} \ll 0$. This leads to the second part of condition (3). In accordance with **Remark 6**, an inductive loop is found at a slightly overbinding catalyst with an overpotential of 0.1 V in Fig. 5.

B. Different transfer coefficients: $\alpha_a \neq \alpha_b$ and $\gamma = 0$

The case of $\alpha_a = \alpha_b = 0.5$ is the exception rather than the rule. It is thus important to analyze whether the above remarks remain valid if $\alpha_a \neq \alpha_b$. For this general case, the rate constants become $k_a^+ = A_0 e^{-\alpha_a(\tilde{E} + \Delta\tilde{G})}$, $k_a^- = A_0 e^{(1-\alpha_a)(\tilde{E} + \Delta\tilde{G})}$, $k_b^+ = A_0 e^{\Delta\tilde{B} - \alpha_b(\tilde{E} - \Delta\tilde{G})}$, and $k_b^- = A_0 e^{\Delta\tilde{B} + (1-\alpha_b)(\tilde{E} - \Delta\tilde{G})}$.

Remark 1 is invalid when $\alpha_a \neq \alpha_b$. This is because Δ_E is nonzero at $\Delta\tilde{B} = 0$ due to the second term, $(k_a^+ k_b^+ - k_a^- k_b^-)(\alpha_a - \alpha_b)$. This means that the EIS shape constitutes, in general, two parts at $\Delta\tilde{B} = 0$. In Fig. 7, various shapes of EIS are observed at $\Delta B = 0$ eV, with other parameters $\alpha_a = 0.7$, $\alpha_b = 0.4$, $\gamma = 0$, $A_0 = 0.1 \ \text{s}^{-1}$, $C_{dl} = 0.1 \ \text{F m}^{-2}$, and $Q = 2 \ \text{C m}^{-2}$. We update **Remark 1** for the case of $\alpha_a \neq \alpha_b$ as follows.

Remark 7. Consider a two-step single-adsorbate electrochemical reaction with $\alpha_a \neq \alpha_b$ and $\gamma = 0$. Its EIS can have various shapes in the Nyquist plot, even if the two steps have equal barriers, namely, $\Delta\tilde{B} = 0$.

Remark 2 is still valid when $\alpha_a \neq \alpha_b$, namely, no inductive loop is expected at the equilibrium potential, regardless of the values of α_a and α_b. At the equilibrium potential, $\tilde{E} = 0$, we have the equality $k_a^+ k_b^+ = k_a^- k_b^-$. Hence, $\Sigma_\theta \Delta_E \propto (k_b^+ k_b^- - k_a^+ k_a^-)(k_b^+ + k_b^- - k_a^+ - k_a^-) > 0$ and all catalysts fall
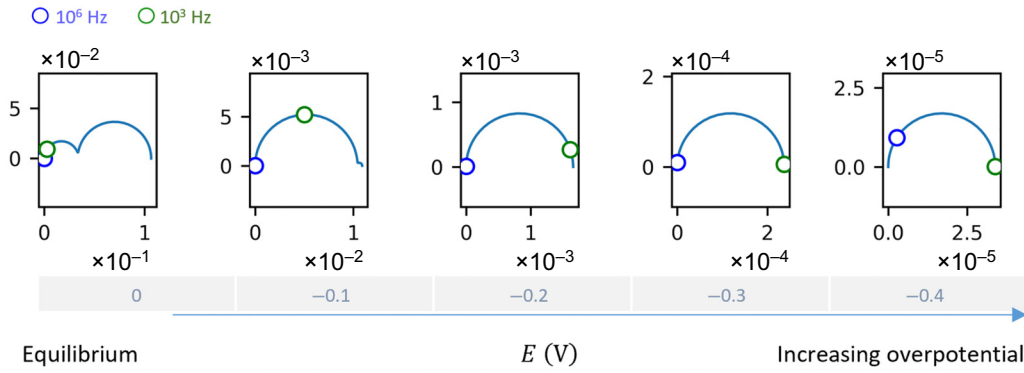
FIG. 6.   EIS shapes of the most active catalysts at different electrode potentials. Parameters are the same as in Fig. 5. Horizontal and vertical axes of the EIS plot represent the real and negative imaginary parts of the impedance (Ωm^2), respectively.

into region 2 in Fig. 2. The mathematical theory of Harrington and van den Driessche also proves that no inductive loop exists at the equilibrium potential [23]. In Fig. 8, no inductive loop is observed in EIS at equilibrium potential. Therefore, **Remark 2** is strengthened a s follows.

Stronger Remark 2. Consider a two-step single-adsorbate electrochemical reaction with $\gamma = 0$. At equilibrium potential, namely, $\tilde{E} = 0$, all catalysts fall into region 2 in Fig. 2. The EIS shape is composed of two semicircles without an inductive loop, regardless of the values of α_a and α_b.

Remark 3 is invalid when $\alpha_a \neq \alpha_b$. In general, the EIS shape is no longer dominated by a single semicircle at high overpotential, and it is possible to observe two semicircles even at high overpotential. Under high overpotential, $|\tilde{E}| \gg \max\{|\Delta\tilde{B}|, |\Delta\tilde{G}|\}$, we can approximate

$$k_a^+ \approx A_0 e^{-\alpha_a \tilde{E}}, k_a^- \approx 0, k_b^+ \approx A_0 e^{-\alpha_b \tilde{E}}, k_b^- \approx 0,$$

$$\Sigma_\theta \approx QA_0(e^{-\alpha_b \tilde{E}} - e^{-\alpha_a \tilde{E}}),$$

$$\Delta_\theta \approx -A_0(e^{-\alpha_b \tilde{E}} + e^{-\alpha_a \tilde{E}}),$$

$$\Sigma_E = -\beta eQ \frac{k_a^+ k_b^+ (\alpha_a + \alpha_b)}{k_a^+ + k_b^+},$$

$$\Delta_E = \beta e \frac{k_a^+ k_b^+ (\alpha_b - \alpha_a)}{k_a^+ + k_b^+}.$$

Therefore, we find

$$\frac{\Sigma_\theta \Delta_E}{\Delta_\theta \Sigma_E} \approx \frac{(\alpha_b - \alpha_a)(e^{-\alpha_b \tilde{E}} - e^{-\alpha_a \tilde{E}})}{(\alpha_a + \alpha_b)(e^{-\alpha_b \tilde{E}} + e^{-\alpha_a \tilde{E}})} \approx \frac{|\alpha_b - \alpha_a|}{\alpha_a + \alpha_b},$$

namely, $0 < (\Sigma_\theta \Delta_E / \Delta_\theta \Sigma_E) < 1$. This means that all catalysts fall into region 2a at high overpotentials and their EIS shapes have two semicircles. The characteristic frequencies of these two semicircles are $\omega_{\text{high}} = (1/C_{\text{dl}})|\Sigma_E|$ and

$$\omega_{\text{low}} = \frac{1}{C_{\text{dl}}} \frac{\alpha_a + \alpha_b - |\alpha_b - \alpha_a|}{\alpha_a + \alpha_b} |\Sigma_E|.$$

When $\Delta\tilde{G} \approx ((\alpha_b - \alpha_a)\tilde{E} - \Delta\tilde{B})/\alpha_a + \alpha_b$, we obtain $k_a^+ \approx k_b^+$, $|\Delta_\theta| \propto \max(k_a^+, k_b^+) \approx |\Sigma_E| \propto \min(k_a^+, k_b^+)$, and $|\Delta_\theta|$ is of the same magnitude as ω_{high} and ω_{low}. The two semicircles can be visibly distinguished. Otherwise, as $|\Delta_\theta| \propto \max(k_a^+, k_b^+) \gg |\Sigma_E| \propto \min(k_a^+, k_b^+)$, thus $|\Delta_\theta| \gg \omega_{\text{high}} > \omega_{\text{low}}$, we can approximate the impedance in the frequency range between ω_{high} and ω_{low} as

$$Z = \frac{1}{j\omega C_{\text{dl}} - ((\Sigma_\theta \Delta_E / j\omega - \Delta_\theta) + \Sigma_E)}$$

$$\approx \frac{1}{j\omega C_{\text{dl}} - (\Sigma_E - (\Sigma_\theta \Delta_E / \Delta_\theta))},$$

implying that the two semicircles melt into one and cannot be visibly distinguished.

In the numerical example provided in Fig. 9, at a high overpotential of $E = -1$ V, we find a two-semicircle impedance shape at $\Delta G = 0.4$ eV when $\Delta G \approx ((\alpha_b - \alpha_a)E - \Delta B)/(\alpha_a + \alpha_b) = 0.54$ eV, and single-semicircle shapes at other values of ΔG. With regard to the volcano plot, the peak activity shifts towards more positive ΔG as the overpotential increases. This implies that kinetically optimal catalysts, compared to the thermodynamically optimal catalyst, vary from one electrode potential to another. A mathematical analysis on the potential dependency of volcano plots was published recently [44,45]. Similar to the case of $\alpha_a = \alpha_b$, the EIS plots for the most active catalysts at different electrode potentials consist of two semicircles without an inductive loop; see Fig. 10. We update **Remark 3** for the case of $\alpha_a \neq \alpha_b$ as follows.
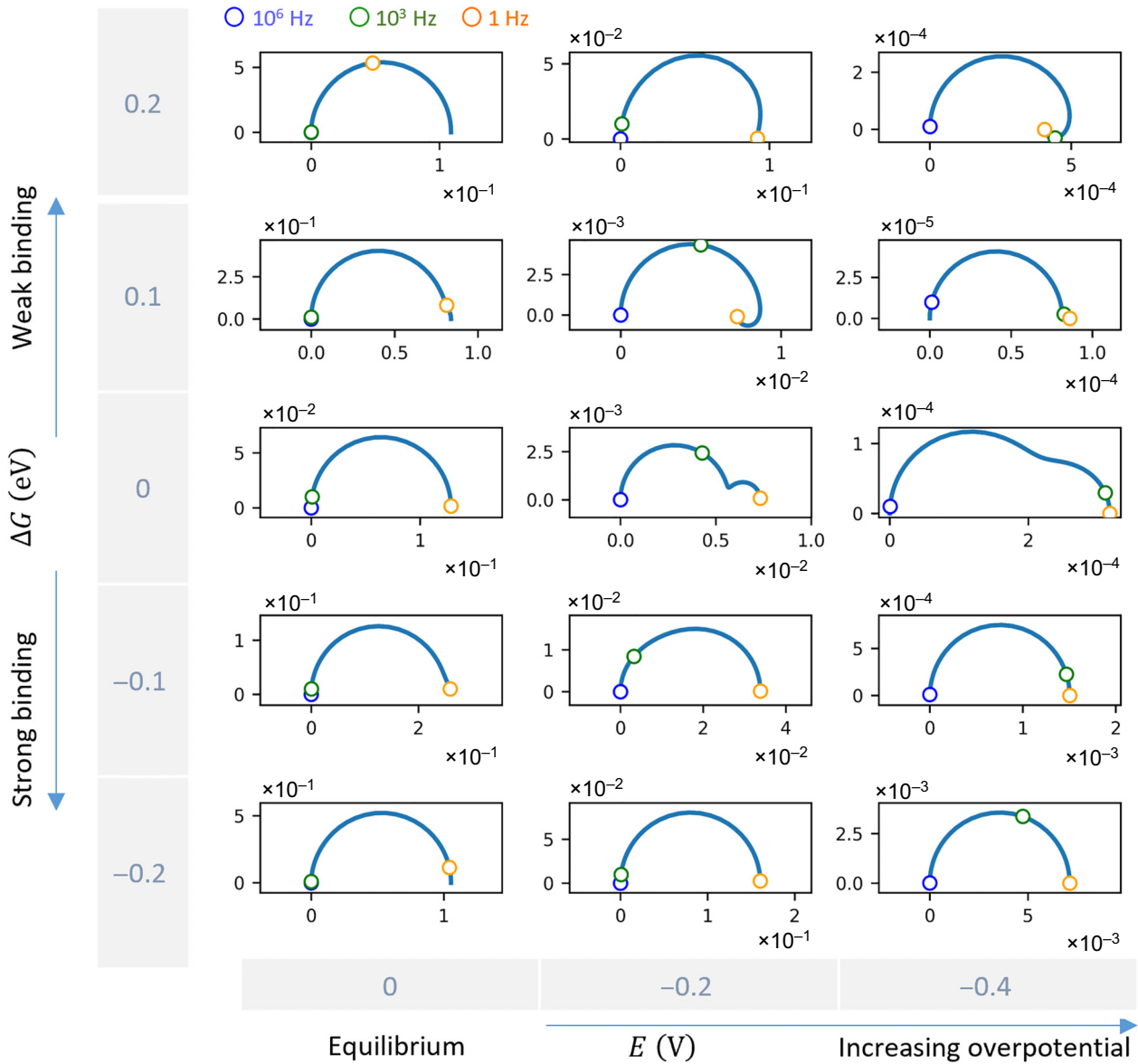
FIG. 7.   EIS shapes at equal barriers $\Delta B = 0$ eV for different transfer coefficients $\alpha_a \neq \alpha_b$. Nyquist plots of EIS at three electrode potentials and five binding energies (ΔG) are obtained with $\alpha_a = 0.7$, $\alpha_b = 0.4$, $\gamma = 0$, $\theta_{\max} = 1$, $A_0 = 0.1$ s^{-1}, $C_{\mathrm{dl}} = 0.1$ F m^{-2}, $Q = 2$ C m^{-2}, $\Delta B = 0$ eV. Horizontal and vertical axes of the EIS plot represent the real and negative imaginary parts of the impedance (Ωm^2), respectively.

Remark 8. Consider a two-step single-adsorbate electrochemical reaction with $\alpha_a \neq \alpha_b$ and $\gamma = 0$. Its EIS shape can have two semicircles at high overpotentials when $\Delta \tilde{G} \approx ((\alpha_b - \alpha_a)\tilde{E} - \Delta \tilde{B})/(\alpha_a + \alpha_b)$. Otherwise, only one semicircle exists.

Remark 4 is also invalid. One can even observe an inductive loop at the thermodynamically optimal catalyst, namely, $\Delta \tilde{G} = 0$, as shown in the example in Fig. 11. In this example, an inductive loop is observed at -0.2 V with parameters listed in the caption.

We update **Remark 4** for the case of $\alpha_a \neq \alpha_b$ as follows.

Remark 9. Consider a two-step single-adsorbate electrochemical reaction with $\alpha_a \neq \alpha_b$ and $\gamma = 0$. The thermodynamically optimal catalyst, namely, $\Delta \tilde{G} = 0$, can have various EIS shapes, including an inductive loop.

Remark 5 remains valid. Consider a two-step single-adsorbate electrochemical reaction with $\alpha_a \neq \alpha_b$ and $\gamma = 0$. *Near equilibrium potential*, inferior catalysts that adsorb the intermediate either very weakly ($\Delta \tilde{G} \gg 0$) or very strongly ($\Delta \tilde{G} \ll 0$) all fall into region 2 in Fig. 2. Hence, the EIS shape is composed of two semicircles without an inductive loop. Otherwise, as $|\Delta_\theta| \propto \max(k_a^+, k_b^+) \gg |\Sigma_E| \propto \min(k_a^+, k_b^+)$, thus $|\Delta_\theta| \gg \omega_{\mathrm{high}} > \omega_{\mathrm{low}}$, implying
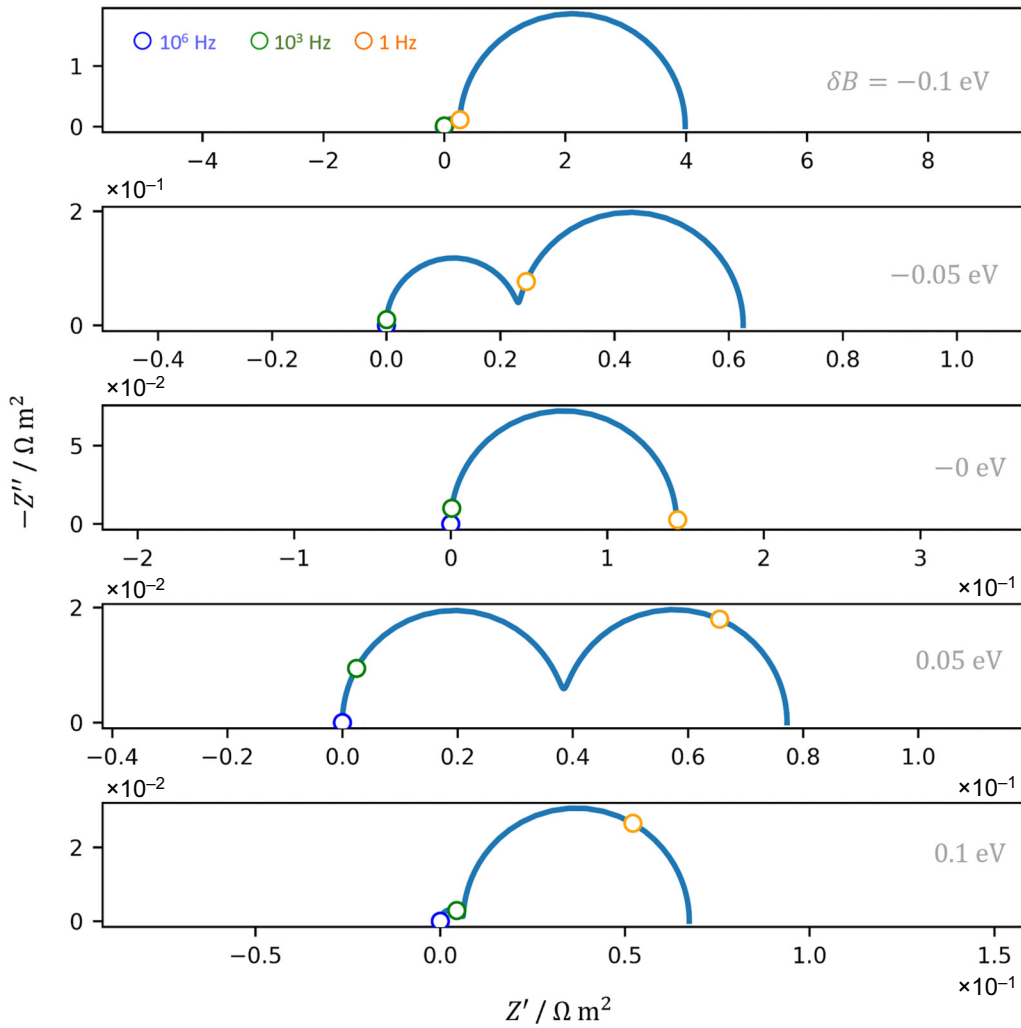
FIG. 8.   EIS shapes at equilibrium potential $E = 0$ V for different transfer coefficients $\alpha_a \neq \alpha_b$. Nyquist plots of EIS at equilibrium potential at five barrier differences (ΔB) are obtained with $\alpha_a = 0.7$, $\alpha_b = 0.4$, $\gamma = 0$, $\theta_{\max} = 1$, $A_0 = 0.1$ s^{-1}, $C_{\mathrm{dl}} = 0.1$ F m^{-2}, $Q = 2$ C m^{-2}. Horizontal and vertical axes of the EIS plot represent the real and negative imaginary parts of the impedance (Ωm^2), respectively.

that the two semicircles melt into a single one and cannot be visibly distinguished; see an example in Fig. 9(b). The EIS plots are composed of one semicircle in the first quadrant.

Let us first consider strongly adsorbing catalysts near equilibrium, $-\Delta \tilde{G} \gg \max\{|\Delta \tilde{B}|, |\tilde{E}|\}$. For this case, we approximate $k_a^+ \approx A_0 e^{-\alpha_a \Delta \tilde{G}}, k_a^- \approx A_0 e^{(1-\alpha_a)\Delta \tilde{G}} \approx 0, k_b^+ \approx A_0 e^{\alpha_b \Delta \tilde{G}} \approx 0, k_b^- = A_0 e^{-(1-\alpha_b)\Delta \tilde{G}}$. The relative magnitudes of k_a^+ and k_b^- depend on $\alpha_a + \alpha_b$. If $\alpha_a + \alpha_b > 1$, we can go further with $k_a^+ \gg k_b^-$, $k_a^- \gg k_b^+$, and thus, $k_a^+ k_a^- \gg k_b^+ k_b^-$. Since $k_a^+ k_a^- - k_b^+ k_b^- \approx e^{(1-2\alpha_a)\Delta \tilde{G}}$ and $k_a^+ k_b^+ - k_a^- k_b^- = e^{\Delta \tilde{B}}(e^{-(\alpha_a+\alpha_b)\tilde{E}} - e^{(2-\alpha_a-\alpha_b)\tilde{E}})e^{-(\alpha_a-\alpha_b)\Delta \tilde{G}}$, we obtain

$$\frac{|k_a^+ k_a^- - k_b^+ k_b^-|}{|k_a^+ k_b^+ - k_a^- k_b^-|} \propto e^{(1-\alpha_a-\alpha_b)\Delta \tilde{G}} \gg 1.$$

Therefore, we obtain $\Sigma_\theta \approx -Qk_a^+ < 0$, $\Delta_\theta \approx -k_a^+ < 0$, $\Delta_E \approx -\beta eQk_a^- < 0$, and $\Sigma_E \approx -\beta ek_a^- < 0$, resulting in $\Sigma_\theta \Delta_E > 0$ and $(\Sigma_\theta \Delta_E / \Delta_\theta \Sigma_E) \approx 1$.

If $\alpha_a + \alpha_b < 1$, we then know $k_a^+ \ll k_b^-$, $k_a^- \ll k_b^+$, $k_a^+ k_a^- \ll k_b^+ k_b^-$, and

$$\frac{|k_a^+ k_a^- - k_b^+ k_b^-|}{|k_a^+ k_b^+ - k_a^- k_b^-|} \propto e^{-(1-\alpha_a-\alpha_b)\Delta \tilde{G}} \gg 1.$$

Therefore, $\Sigma_\theta \approx Qk_b^- > 0$, $\Delta_\theta \approx -k_b^- < 0$, $\Sigma_E \approx -\beta eQk_b^+ < 0$, and $\Delta_E \approx \beta ek_b^+ > 0$, so that $\Sigma_\theta \Delta_E > 0$ and $(\Sigma_\theta \Delta_E / \Delta_\theta \Sigma_E) \approx 1$. Repeating the same analysis for the weakly adsorbing catalysts near equilibrium potential, we find that the same conclusion still holds true.

Therefore, **Remark 5** is strengthened as follows.

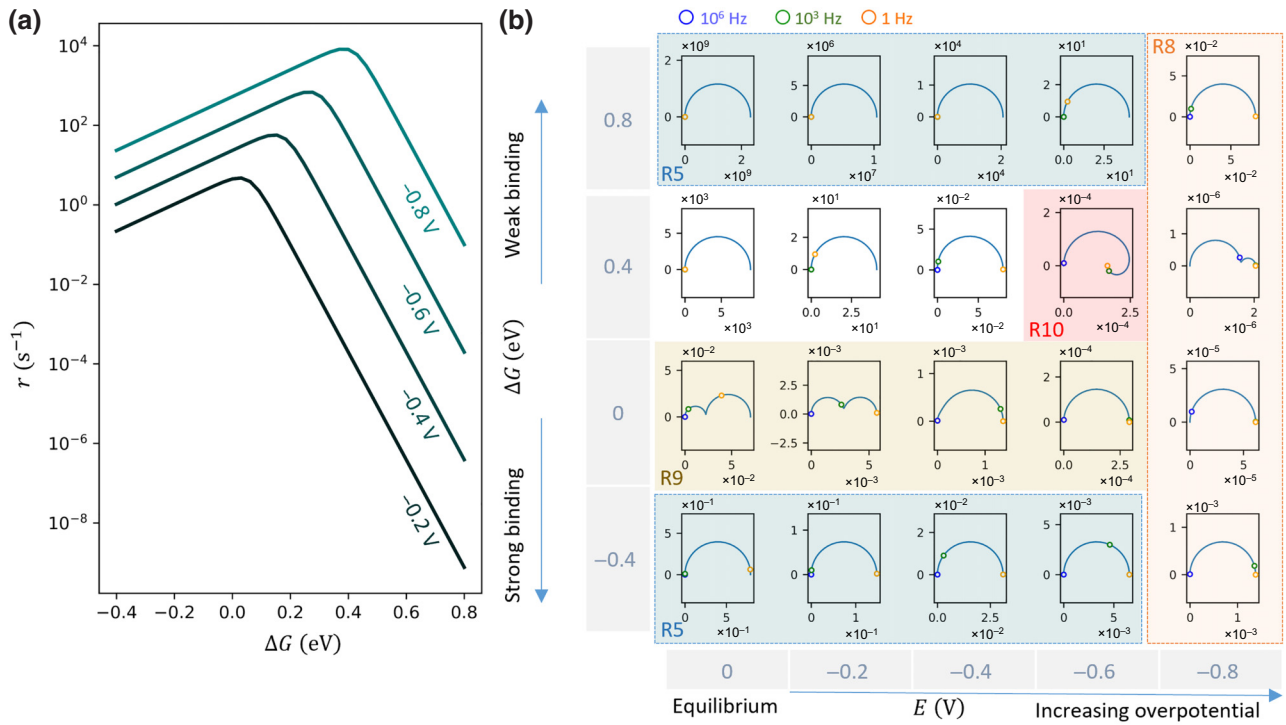**Stronger Remark 5.** Consider a two-step single-adsorbate electrochemical reaction with $\gamma = 0$. Catalysts

FIG. 9. Correlation between EIS shapes and activity for the single-adsorbate reaction with different transfer coefficients $\alpha_a \neq \alpha_b$. (a) Volcano plots of activity and (b) Nyquist plots of EIS at different electrode potentials and binding energies (ΔG) are obtained with parameters, $\alpha_a = 0.8$, $\alpha_b = 0.2$, $\gamma = 0$, $\theta_{max} = 1$, $A_0 = 0.1 \text{ s}^{-1}$, $C_{dl} = 0.1 \text{ F m}^{-2}$, $Q = 2 \text{ C m}^{-2}$, $\Delta B = 0.06$ eV. Horizontal and vertical axes of the EIS plot represent the real and negative imaginary parts of the impedance (Ωm^2), respectively. "R" is short for "Remark."

that adsorb the intermediate very weakly ($\Delta \tilde{G} \gg 0$) or very strongly ($\Delta \tilde{G} \ll 0$), namely, low-activity catalysts, possess only one semicircle, and no inductive loop is expected, regardless of the values of α_a and α_b.

Combined, **Remark 6** regarding necessary conditions to observe an inductive loop in the low-frequency range should be modified for the case of $\alpha_a \neq \alpha_b$ as follows.

Remark 10. Consider a two-step single-adsorbate electrochemical reaction with $\alpha_a \neq \alpha_b$ and $\gamma = 0$. Necessary conditions to observe an inductive loop in the

low-frequency range include (1) the reaction intermediate is adsorbed not too strongly or weakly; and (2) the overpotential is nonzero but not too high.

In comparison with the case of $\alpha_a = \alpha_b$, the constraints are fewer. However, as shown in Fig. 9, it is still rare to observe an inductive loop.

C. Effect of lateral interactions $\gamma \neq 0$

Now we further release the assumption of $\gamma = 0$ and examine how lateral interactions of intermediates influence
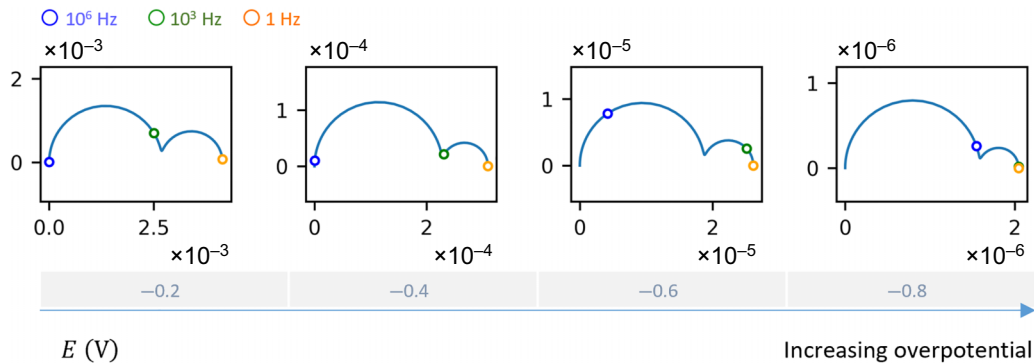

FIG. 10. EIS shapes of the most active catalysts at different electrode potentials. Parameters are the same as in Fig. 9. Horizontal and vertical axes of EIS plot represent the real and negative imaginary parts of the impedance (Ωm^2), respectively.
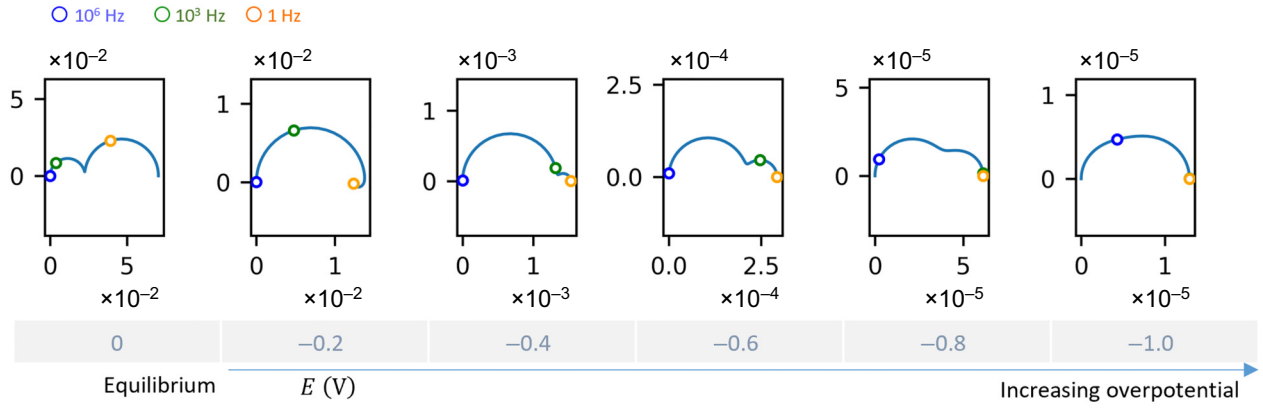
FIG. 11. EIS shapes for the thermodynamically optimal catalyst, $\Delta G = 0$ eV, with different transfer coefficients $\alpha_a \neq \alpha_b$. Other parameters are $\alpha_a = 0.4$, $\alpha_b = 0.2$, $\gamma = 0$, $\theta_{\max} = 1$, $A_0 = 0.1$ s^{-1}, $C_{\mathrm{dl}} = 0.1$ F m^{-2}, $Q = 2$ C m^{-2}, $\Delta B = 0.06$ eV. Horizontal and vertical axes of the EIS plot represent the real and negative imaginary parts of the impedance (Ωm^2), respectively.

the EIS shapes. In Table I, experimental data of under-potential deposition of hydrogen (H$_{\mathrm{UPD}}$) and hydroxyl adsorption on platinum single crystals in acidic and alkaline solutions are listed. In most scenarios, lateral interactions are repulsive, namely, $\gamma > 0$. Attractive lateral interactions with $\gamma < 0$ are found in OH adsorption on Pt(111) at high coverages and H$_{\mathrm{UPD}}$ on Pt(110) in 0.1M HClO$_4$.

Remark 11. Consider a two-step single-adsorbate electrochemical reaction. The influence of lateral interactions is negligible at weakly binding catalysts with $\Delta G \gg 0$.

At weakly binding catalysts with $\Delta G \gg 0$, the coverage θ is nearly zero, and all reaction rate constants, $k_{a,b}^{\pm}$, are then not changed by γ. In addition, since Σ_E and Δ_E approaches zero at $\Delta G \gg 0$, as seen from Eqs. (32) and (33),

$$\Sigma_\theta = Q(k_b^+ + k_b^- - k_a^+ - k_a^-) + \gamma \Delta_E \approx Q(k_b^+ + k_b^- - k_a^+ - k_a^-)$$

and

$$\Delta_\theta = -k_a^+ + k_a^- + k_b^+ + k_b^- + \frac{\gamma \Sigma_E}{Q} \approx -k_a^+ + k_a^- + k_b^+ + k_b^-.$$

Therefore, the EIS plots do not change with γ.

In Fig. 12, EIS plots are shown at different potentials and binding energies for $\gamma = -0.2$ V, $\gamma = 0$, and $\gamma = 0.2$ V, with parameters $\alpha_a = 0.8$, $\alpha_b = 0.2$, $\theta_{\max} = 1$, $A_0 = 0.1$ s^{-1}, $C_{\mathrm{dl}} = 0.1$ F m^{-2}, $Q = 2$ C m^{-2}, and $\Delta B = 0.06$ eV. EIS plots at three values of γ almost overlap for $\Delta G = 0.4$ eV, namely, at weakly binding catalysts. It is worth noting that EIS plots are also insensitive to γ for strongly binding catalysts, namely, $\Delta G = -0.4$ eV, for $\theta = \theta_a = \theta_b \approx 1$ and the k values do not change with γ.

Remark 12. Consider a two-step single-adsorbate electrochemical reaction. Regime 4b, where the EIS shape is

composed of a semicircle in the first quadrant followed by an inverse semicircle in the fourth quadrant extending further along the x axis, is possible, and its occurrence indicates attractive lateral interactions. Regime 4b, if it exists, is limited to the near-equilibrium potential region at close-to-optimal catalysts.

Regime 4b requires $\Delta_\theta > 0$ and $\Sigma_E \Delta_\theta < \Sigma_\theta \Delta_E < -C_{\mathrm{dl}} \Delta_\theta^2$. Since $\Delta_\theta = -(k_a^+ + k_a^- + k_b^+ + k_b^-) + (\gamma \Sigma_E / Q)$ and Σ_E is always negative, positive Δ_θ is admissible only when $\gamma < 0$, namely, attractive lateral interactions, and $(k_a^+ + k_a^- + k_b^+ + k_b^-)$ has a lower magnitude than $\gamma \Sigma_E / Q$. Since $k_a^+ + k_a^- + k_b^+ + k_b^-$ grows exponentially with the over-potential and the magnitude of ΔG, the second condition is more likely to be met when the overpotential is lower at close-to-optimal catalysts.

The EIS shape belonging to regime 4b is observed at $\Delta G = 0$, $E = 0$, and $\gamma = -0.2$ V in Fig. 12. In addition, for other sets of ΔG and E, we observe that γ only changes the magnitude of EIS without altering the shape.

V. AN EXTENDED MODEL

In the preceding sections, we have presented a complete regime diagram of shapes of impedance plots for a two-step single-adsorbate reaction and explored the correlation between electrocatalytic activity and impedance shape. It is thus natural to ask whether the conclusions apply for more complicated reactions or not. To address this question, we are about to present an extended EIS model of electrocatalytic reactions in this section, followed by demystification and simplification of the extended formalism in subsequent sections. Such a practice of deriving EIS for a given reaction mechanism dates back to the earliest days of EIS [11,13]. The derivation presented below follows the routine established in these works.
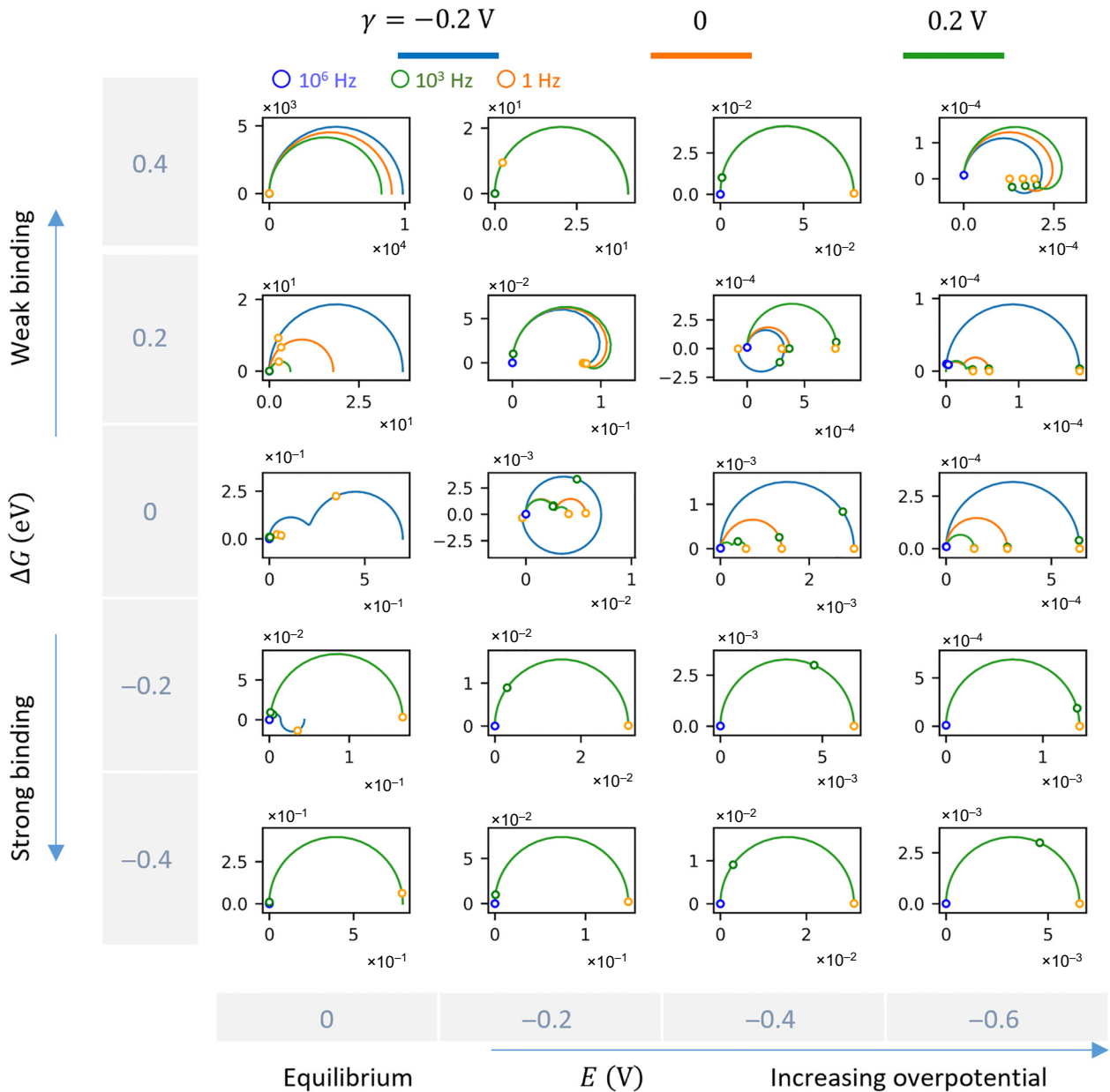
FIG. 12. Influence of lateral interactions on the EIS shapes. Nyquist plots of EIS for a two-step single-adsorbate electrochemical reaction at different electrode potentials and binding energies (ΔG) are obtained with parameters, $\alpha_a = 0.8$, $\alpha_b = 0.2$, $\theta_{\max} = 1$, $A_0 = 0.1$ s^{-1}, $C_{\mathrm{dl}} = 0.1$ F m^{-2}, $Q = 2$ C m^{-2}, $\Delta B = 0.06$ eV. Horizontal and vertical axes of the EIS plot represent the real and negative imaginary parts of the impedance (Ωm^2), respectively. PYTHON code for generating this figure is provided in the Supplemental Material [43].

Consider a multistep electrocatalytic reaction that proceeds via N elementary steps involving M adsorbed intermediates and P solution-phase species. The elementary step indexed with i is written generally as

$$\left(\sum_{p=1}^{P} a_{ip} R_p\right) + \left(\sum_{m=1}^{M} b_{im} I_m\right) + c_i * + n_i e = 0, \quad (42)$$

where R_p represents solution-phase species with the stoichiometric number a_{ip}, I_m represents adsorbed

intermediates with the stoichiometric number b_{im}, n_i is the number of electrons involved this step, $*$ indicates vacant sites, and c_i is the number of vacant sites involved in this step.

The rate of change of coverage of intermediate I_m, denoted θ_m, is calculated as

$$\frac{d\theta_m}{dt} = -\sum_{i=1}^{N} b_{im} v_i. \quad (43)$$

The reaction rate of the step i, v_i, is, in general, a function of the electrode potential, E; interfacial concentration of R_p, denoted C_p; and θ_m:

$$v_i = v_i(E, C_1, \ldots, C_P, \theta_1, \ldots, \theta_m). \quad (44)$$

The total differential of v_i is obtained as

$$
\tilde{v}_i = \left(\frac{\partial v_i}{\partial E}\right)_{\{C_k\},\{\theta_k\}} \tilde{E} + \sum_{p=1}^{P} \left(\frac{\partial v_i}{\partial C_p}\right)_{E,\{C_k(k\neq p)\},\{\theta_k\}} \tilde{C}_p
$$
$$
+ \sum_{m=1}^{M} \left(\frac{\partial v_i}{\partial \theta_m}\right)_{E,\{C_k\},\{\theta_k(k\neq m)\}} \tilde{\theta}_m, \quad (45)
$$

where $\{C_k\}$ is short for $(C_1, \ldots, C_P)$, $\{\theta_k\}$ for $(\theta_1, \ldots, \theta_M)$, $\{C_k(k \neq p)\}$ for $(C_1, \ldots, C_{p-1}, C_{p+1}, \ldots, C_P)$, and $\{\theta_k (k \neq m)\}$ for $(\theta_1, \ldots, \theta_{m-1}, \theta_{m+1}, \ldots, \theta_M)$.

Controlled by mass transport in the electrolyte solution, C_p is described as

$$\frac{dC_p}{dt} = D_p \frac{d^2 C_p}{dx^2}, \quad (46)$$

which is transformed into $j\omega\tilde{C}_p = D_p(d^2\tilde{C}_p/dx^2)$ in the frequency space, closed with boundary conditions $\tilde{C}_p = 0$ in the bulk solution, $x = l$, and

$$D_p \frac{d\tilde{C}_p}{dx} = N_{as} \sum_{i=1}^{N} \tilde{v}_i a_{ip},$$

at the reaction plane, $x = 0$. Here, $N_{as} = Q/F$ is the molar number density of active sites.

The general solution to this second-order differential equation is

$$\tilde{C}_p(x) = f_1 \exp\left(x\sqrt{\frac{j\omega}{D_p}}\right) + f_2 \exp\left(-x\sqrt{\frac{j\omega}{D_p}}\right). \quad (47)$$

We have $f_1 = -f_2 \exp\left(-2l\sqrt{j\omega/D_p}\right)$ due to the condition of $\tilde{C}_p = 0$ at $x = l$. The other condition then gives

$$f_2 = -\frac{N_{as} \sum_{i=1}^{N} \tilde{v}_i a_{ip}}{\sqrt{j\omega D_p}} \frac{1}{\left(\exp\left(-2l\sqrt{j\omega/D_p}\right) + 1\right)}.$$

The interfacial concentration at $x = 0$ is now

$$
\tilde{C}_p = \frac{N_{as} \sum_{i=1}^{N} \tilde{v}_i a_{ip}}{\sqrt{j\omega D_p}} \frac{\exp\left(-2l\sqrt{j\omega/D_p}\right) - 1}{\exp\left(-2l\sqrt{j\omega/D_p}\right) + 1}
$$
$$
= -\frac{N_{as} \sum_{i=1}^{N} \tilde{v}_i a_{ip}}{\sqrt{j\omega D_p}} \tanh\left(l\sqrt{\frac{j\omega}{D_p}}\right). \quad (48)
$$

Substituting Eq. (48) back into (45) leads to

$$
\tilde{v}_i + \sum_{p=1}^{P} \left(\frac{\partial v_i}{\partial C_p}\right)_{u,\{C_k(k\neq p)\},\{\theta_k\}} \frac{N_{as} \sum_{q=1}^{N} a_{qp}\tilde{v}_q}{\sqrt{j\omega D_p}} \tanh\left(l\sqrt{\frac{j\omega}{D_p}}\right)
$$
$$
= \left(\frac{\partial v_i}{\partial E}\right)_{\{C_k\},\{\theta_k\}} \tilde{E} + \sum_{m=1}^{M} \left(\frac{\partial v_i}{\partial \theta_m}\right)_{u,\{C_k\},\{\theta_k(k\neq m)\}} \tilde{\theta}_m, \quad (49)
$$

Introducing the following matrices and vectors, of which the dimension is specified in the superscript,

$$
\mathbf{D}^{N\times P}(i,p) = \frac{N_{as}}{\sqrt{j\omega D_p}} \left(\frac{\partial v_i}{\partial C_p}\right)_{E,\{C_k(k\neq p)\},\{\theta_k\}} \tanh\left(l\sqrt{\frac{j\omega}{D_p}}\right),
$$
$$
\mathbf{A}^{N\times P}(q,p) = a_{qp},
$$
$$
\mathbf{K}_\theta^{N\times M}(i,m) = \left(\frac{\partial v_i}{\partial \theta_m}\right)_{E,\{C_k\},\{\theta_k(k\neq m)\}},
$$
$$
\mathbf{K}_E^{N\times 1}(i) = Q\left(\frac{\partial v_i}{\partial E}\right)_{\{C_k\},\{\theta_k\}},
$$
$$
\tilde{\theta}^{M\times 1}(m) = \tilde{\theta}_m,
$$
$$
\tilde{\mathbf{v}}^{N\times 1}(i) = \tilde{v}_i, \quad (50)
$$

we write Eq. (49) in a concise matrix form:

$$
(\mathbf{I}^{N\times N} + \mathbf{D}\mathbf{A}^T)\tilde{\mathbf{v}} = \frac{\mathbf{K}_u}{Q}\tilde{E} + \mathbf{K}_\theta \tilde{\theta},
$$
$$
\tilde{\mathbf{v}} = \frac{\mathbf{k}_u'}{Q}\tilde{E} + \mathbf{K}_\theta' \tilde{\theta}, \quad (51)
$$

TABLE I. Experimental data of underpotential deposition of hydrogen (H_{UPD}) and hydroxyl adsorption on platinum single crystals in acidic and alkaline solutions.

Adsorption process	γ	Ref.
H_{UPD} on Pt(111) in 0.1M HClO$_4$	0.29–0.34 V at 276–333 K	[46]
H_{UPD} on Pt(111) in 0.1M NaOH	0.37–0.39 V at 276–333 K	
H_{UPD} on Pt(111) in 0.05M H$_2$SO$_4$	0.32–0.34 V at 276–333 K	
H_{UPD} on Pt(111) in 0.1M HClO$_4$	0.29 V at 276–333 K	[47]
H_{UPD} on Pt(100) in 0.1M HClO$_4$	0.09 V at 276–333 K	
H_{UPD} on Pt(110) in 0.1M HClO$_4$	-0.04 V at 276–333 K	
H_{UPD} on Pt(111) in 0.05M NaOH	0.21 V at 313 K	[48]
OH adsorption on Pt(111) in 0.1M HClO$_4$	0.1–0.15 V when $\theta_{OH} < 0.5$, negative when $\theta_{OH} > 0.6$ at 273–323 K	[49]
OH adsorption on Pt(100) in 0.1 M HClO$_4$	0.14 V at 313 K	

with diffusion-corrected terms $\overset{'}{\mathbf{K}}_u = (\mathbf{I} + \mathbf{DA}^T)^{-1}\mathbf{K}_E$ and $\overset{'}{\mathbf{K}}_\theta = (\mathbf{I} + \mathbf{DA}^T)^{-1}\mathbf{K}_\theta$. The superscript T means transpose.

Following the procedure for the previous single-adsorbate case, from Eq. (43) we obtain

$$j\omega\tilde{\theta}_m = -\sum_{i=1}^{N} b_{im}\tilde{v}_i. \tag{52}$$

Substituting Eq. (51) for $\tilde{v}_i$ and introducing $\mathbf{B}^{N\times M}(i,m) = b_{im}$, we obtain

$$\left(j\omega\mathbf{I}^{M\times M} + \mathbf{B}^T\overset{'}{\mathbf{K}}_\theta\right)\tilde{\theta} = -\frac{\mathbf{B}^T\overset{'}{\mathbf{K}}_u}{Q}\tilde{E},$$
$$\tilde{\theta} = -\frac{1}{Q}\left(j\omega\mathbf{I} + \mathbf{B}^T\overset{'}{\mathbf{K}}_\theta\right)^{-1}\mathbf{B}^T\mathbf{K}_E\tilde{E}. \tag{53}$$

The Faradaic current density is written as

$$\begin{aligned}
\tilde{i}_{\text{ct}} &= -Q\sum_{i=1}^{N}n_i\tilde{v}_i = -Q\mathbf{n}^T\tilde{\mathbf{v}} = -\mathbf{n}^T\left(\overset{'}{\mathbf{K}}_u\tilde{E} + \overset{'}{\mathbf{K}}_\theta\tilde{\theta}\right), \\
&= -\mathbf{n}^T\left(-\overset{'}{\mathbf{K}}_\theta\left(j\omega\mathbf{I} + \mathbf{B}^T\overset{'}{\mathbf{K}}_\theta\right)^{-1}\mathbf{B}^T\mathbf{K}_E + \overset{'}{\mathbf{K}}_E\right)\tilde{E},
\end{aligned} \tag{54}$$

where $\mathbf{n}$ is the vector of electron numbers. Elements of $\mathbf{n}$ take one of three values $0, \pm 1$.

The impedance response is then written as

$$Z = \frac{\tilde{u}}{\tilde{i}_{\text{dl}} + \tilde{i}_{\text{ct}}} = \left(j\omega C_{\text{dl}} - \mathbf{n}^T\left(\mathbf{I} - \overset{'}{\mathbf{K}}_\theta\left(j\omega\mathbf{I} + \mathbf{B}^T\overset{'}{\mathbf{K}}_\theta\right)^{-1}\mathbf{B}^T\right)\overset{'}{\mathbf{K}}_E\right)^{-1}. \tag{55}$$

To put Eq. (55) into practical use, we need to know $\overset{'}{\mathbf{K}}_\theta$ and $\overset{'}{\mathbf{K}}_E$, which depend on the steady-state conditions. As in the previous example of a single-adsorbate reaction, we need to solve for $\{\bar{\theta}_k\}$ under steady-state conditions from a proper microkinetic model.

The general expression of elementary reaction rates, v_i, in Eq. (44) can be concretely expressed as

$$v_i = k_i^+\prod_{P(\{a_{ip}\},\{b_{ip}\},c_i)}C_R^{r_R} - k_i^-\prod_{N(\{a_{ip}\},\{b_{ip}\},c_i)}C_P^{r_P} \tag{56}$$

where $P(\{a_{ip}\}, \{b_{ip}\}, c_i)$ represents the group of reactants, namely, species with positive stoichiometry number in the reaction in Eq. (42), and $N(\{a_{ip}\}, \{b_{ip}\}, c_i)$ is the group of products, namely, species with negative stoichiometry number. The concentration (coverage) of the reactants and products are denoted C_R and C_P, respectively. The reaction orders of the reactants and products are denoted r_R and r_P, respectively.

To see how the formalism works, we take as an example $O_2 + H^+ - OOH_{\text{ad}} + e + * = 0$, which is usually written as $O_2 + H^+ + e + * = OOH_{\text{ad}}$. The solution-phase reactants are O_2 and H^+, both with a stoichiometry number of unity, and the product is OOH_{ad}. For this step, we have $\{a_{ip}\} = \{1,1\}$, $\{b_{ip}\} = \{-1\}$, $c_i = 1$, $n_i = 1$. Therefore, Eq. (56) becomes $v_i = k_i^+ C_{O_2}C_{H^+}\theta_* - k_i^-\theta_{OOH}$.

The rate constants are given by

$$k_i^+ = k_0\exp\left(-\frac{\Delta G_{a,i} + \alpha_i n_i F(E - E_{\text{eq},i})}{RT}\right),$$
$$k_i^- = k_0\exp\left(-\frac{\Delta G_{a,i} + (1-\alpha_i)n_i F(E - E_{\text{eq},i})}{RT}\right), \tag{57}$$

with k_0 being the exponential prefactor, $\Delta G_{a,i}$ the activation barrier under equilibrium, α_i the transfer coefficient, and $E_{\text{eq},i}$ the equilibrium potential. We have neglected the lateral interaction between adsorbates here.

Under steady states, the coverages do not change with time:

$$\frac{d\theta_m}{dt} = -\sum_{i=1}^{N}b_{im}v_i = 0, \tag{58}$$

and the sum of all coverages is conserved:

$$\theta_* + \sum_{m=1}^{M}\theta_m = 1. \tag{59}$$

Substituting Eq. (56) for v_i in Eq. (58), we obtained all $\bar{\theta}_m$ at a certain electrode potential E. Then, we could obtain all elements of $\overset{'}{\mathbf{K}}_\theta$ and $\overset{'}{\mathbf{K}}_E$ according to Eq. (50). One is then ready to compute EIS using Eq. (55).

VI. APPLICATION OF THE EXTENDED MODEL

In this section, we take the mechanism of formic acid oxidation as an example to illustrate how the extended

formulism works. Formic acid oxidation is assumed to occur via the following simplified mechanism (cf. detailed discussion on possible mechanisms in Refs. [50–52]):

$$\text{HCOOH} + {}^* = \text{HCOO}_{ad} + \text{H}^+ + e,$$
$$\text{HCOO}_{ad} = \text{CO}_2 + \text{H}^+ + e + {}^*. \tag{60}$$
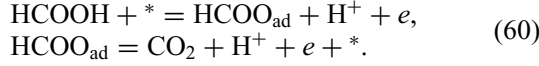
For this case, we have two elementary steps ($N = 2$), three solution-phase species $P = 3$, and one adsorbed intermediate $M = 1$. The matrices are

$$\mathbf{A} = \begin{bmatrix} 1 & -1 & 0 \\ 0 & -1 & -1 \end{bmatrix}, \mathbf{B} = \begin{bmatrix} -1 \\ 1 \end{bmatrix}, \mathbf{C} = \begin{bmatrix} 1 \\ -1 \end{bmatrix},$$

$$\mathbf{n} = \begin{bmatrix} -1 \\ -1 \end{bmatrix}. \tag{61}$$

The reaction rates are

$$v_1 = k_1^+ C_1 \theta_* - k_1^- C_2 \theta_1,$$
$$v_2 = k_2^+ \theta_1 - k_2^- C_3 C_2 \theta_*, \tag{62}$$

where C_1, C_2, and C_3 are the concentrations of HCOOH, H^+, and CO_2, respectively.

According to the steady state expressed in Eq. (58), we obtain

$$\bar{\theta}_1 = \frac{k_1^+ C_1 + k_2^- C_3 C_2}{k_1^+ C_1 + k_1^- C_2 + k_2^+ + k_2^- C_3 C_2},$$

$$\bar{\theta}_* = \frac{k_1^- C_2 + k_2^+}{k_1^+ C_1 + k_1^- C_2 + k_2^+ + k_2^- C_3 C_2}. \tag{63}$$

Then, according to the definitions given in Eq. (50), we obtain $\mathbf{D}, \mathbf{K}_\theta, \ \mathbf{K}_E$ as

$$\mathbf{D} = \begin{bmatrix} k_1^+ \bar{\theta}_* W_1 & -k_1^- \bar{\theta}_1 W_2 & 0 \\ 0 & -k_2^- \bar{C}_3 \bar{\theta}_* W_2 & -k_2^- \bar{C}_2 \bar{\theta}_* W_3 \end{bmatrix},$$

$$\mathbf{K}_\theta = \begin{bmatrix} -k_1^+ \bar{C}_1 - k_1^- \bar{C}_2 \\ k_2^+ + k_2^- \bar{C}_3 \bar{C}_2 \end{bmatrix},$$

$$\mathbf{K}_E = \mathbf{Q} \begin{bmatrix} \bar{C}_1 \bar{\theta}_* \frac{\partial k_1^+}{\partial E_M} - \bar{C}_2 \bar{\theta}_1 \frac{\partial k_1^-}{\partial E_M} \\ \bar{\theta}_1 \frac{\partial k_2^+}{\partial E_M} - \bar{C}_3 \bar{C}_2 \bar{\theta}_* \frac{\partial k_2^-}{\partial E_M} \end{bmatrix}, \tag{64}$$

where

$$W_i = \frac{N_{as}}{\sqrt{j\omega D_p}} \tanh\left(l\sqrt{\frac{j\omega}{D_p}}\right)$$

are the finite-length Warburg elements.

With $\mathbf{K}'_E = (\mathbf{I} + \mathbf{DA}^T)^{-1}\mathbf{K}_E$ and $\mathbf{K}'_\theta = (\mathbf{I} + \mathbf{DA}^T)^{-1}\mathbf{K}_\theta$, and the following manipulation,

$$\left(\mathbf{I} - \mathbf{K}'_\theta\left(j\omega\mathbf{I} + \mathbf{B}^T\mathbf{K}'_\theta\right)^{-1}\mathbf{B}^T\right) = \mathbf{I} - \frac{1}{j\omega - \mathbf{K}'_\theta(1) + \mathbf{K}'_\theta(2)}\begin{bmatrix} -\mathbf{K}'_\theta(1) & \mathbf{K}'_\theta(1) \\ -\mathbf{K}'_\theta(2) & \mathbf{K}'_\theta(2) \end{bmatrix},$$

$$= \frac{1}{j\omega - \mathbf{K}'_\theta(1) + \mathbf{K}'_\theta(2)}\begin{bmatrix} j\omega + \mathbf{K}'_\theta(2) & -\mathbf{K}'_\theta(1) \\ \mathbf{K}'_\theta(2) & j\omega - \mathbf{K}'_\theta(1) \end{bmatrix},$$

the interfacial impedance expressed in Eq. (55) is rewritten as

$$Z = \left(j\omega C_{dl} + \frac{j\omega\left(\mathbf{K}'_E(1) + \mathbf{K}'_E(2)\right) + 2\mathbf{K}'_\theta(2)\mathbf{K}'_E(1) - 2\mathbf{K}'_\theta(1)\mathbf{K}'_E(2)}{j\omega - \mathbf{K}'_\theta(1) + \mathbf{K}'_\theta(2)}\right)^{-1}, \tag{65}$$

which is rewritten in the form of Eq. (11) as

$$Z = \frac{1}{j\omega C_{dl} - ((\Sigma_\theta \Delta_E / j\omega - \Delta_\theta) + \Sigma_E)}, \tag{66}$$

with $\Delta_\theta = \mathbf{K}'_\theta(1) - \mathbf{K}'_\theta(2)$, $\Sigma_E = -\mathbf{K}'_E(1) - \mathbf{K}'_E(2)$, $\Sigma_\theta = \mathbf{K}'_\theta(1) - \mathbf{K}'_\theta(2)$, and $\Delta_E = -\mathbf{K}'_E(1) + \mathbf{K}'_E(2)$.

In Fig. 13, Nyquist plots of EIS for the formic acid oxidation reaction following the mechanism in Eq. (60) are shown at different adsorption energies of the adsorbed intermediate OOH_{ad} and different overpotentials. Lines in orange correspond to the case without considering the diffusion of HCOOH, H^+, and CO_2 in the electrolyte solution, while those in blue consider these diffusion processes. Both types of lines overlap, and the two cases cannot be visibly distinguished in the high-moderate frequency range. When diffusion is considered, additional features, namely, an inclined line of 45° transiting to a semicircle, manifest in the low-frequency range. These additional features are well-established for finite-length diffusion; see an experimental example in Ref. [53]. A key insight from this comparison states that one can obtain the full impedance by combining diffusion impedance and
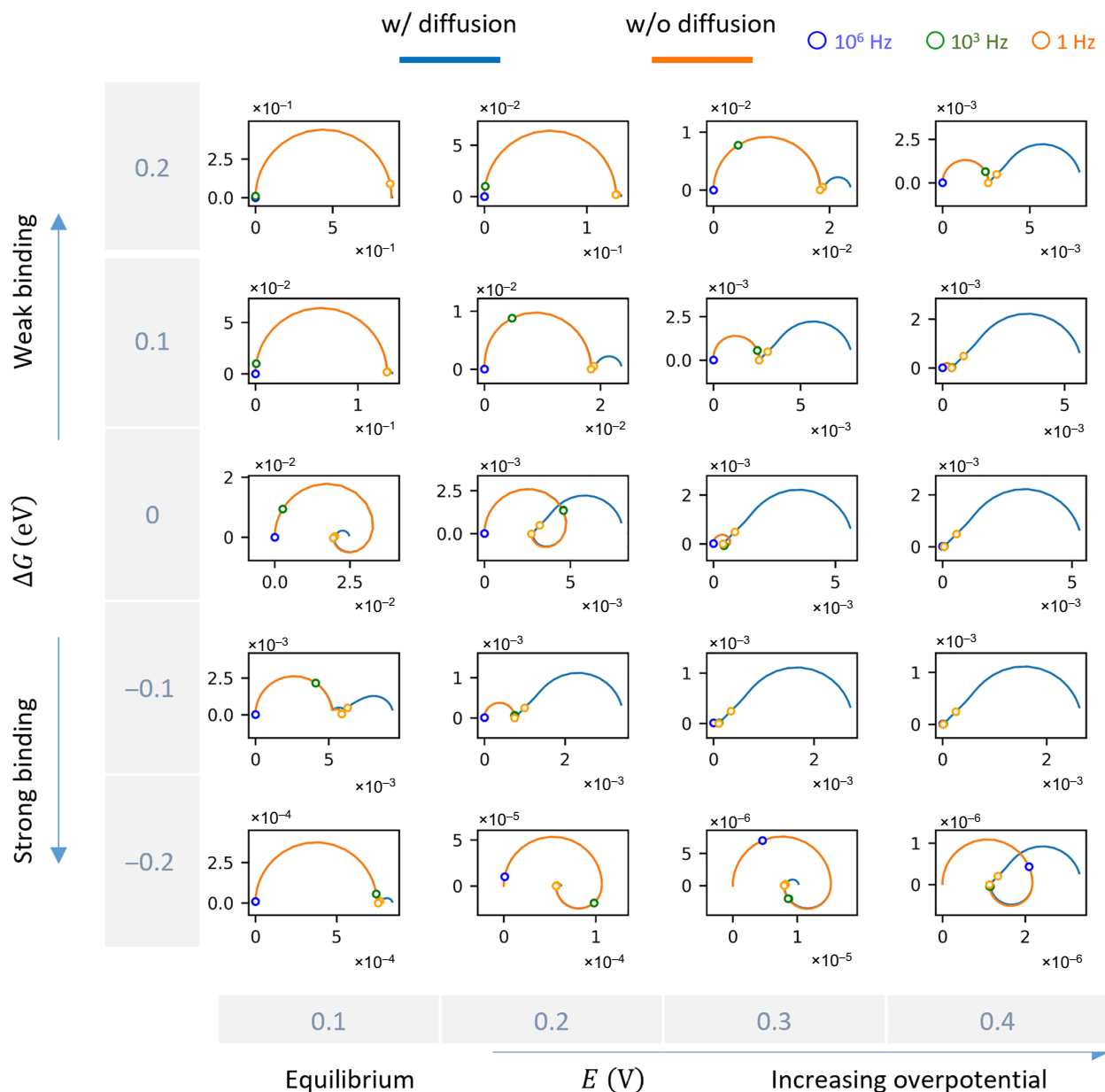
FIG. 13.   Diffusion effects on EIS shapes. Nyquist plots of EIS for formic acid oxidation reaction following the mechanism in Eq. (60) at different adsorption energies of the adsorbed intermediate OOH_{ad} and different overpotentials. Lines in orange correspond to the case without considering diffusion of HCOOH, H^+, and CO_2 in the electrolyte solution, while those in blue consider diffusion. Both types of lines overlap in the high-moderate frequency range. Diffusion only manifests in the low-frequency range as an inclined line of 45° transiting to a semicircle, which are characteristic features of finite-length diffusion. PYTHON code for generating this figure is provided in the Supplemental Material [43].

Faradaic impedance. Diffusion will not alter the preceding analysis on the correlation between EIS shapes and catalytic activity.

Back in 1972, Armstrong and Henderson included the diffusion of the reactant and product dissolved in the electrolyte solution in their impedance model [13]. They considered infinite-length diffusion processes, resulting in Warburg elements $(j\omega D_i)^{-0.5}$ in the impedance expressions. Consistent with our above findings, they revealed that the impedance expression with diffusion reduces back to that without diffusion in the high-frequency range. Lasia derived an impedance model for the hydrogen evolution reaction and considered the diffusion of dissolved hydrogen molecules in the electrolyte solution with a finite length [37,38]. Lasia's results show the same diffusion features as those in Fig. 13.
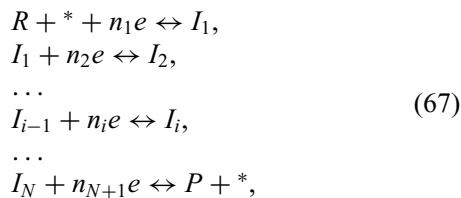
The analysis presented in this section can be summarized in the following remark.

Remark 13. Reaction and diffusion are usually well separated in the electrochemical impedance plots and located in the high- and low-frequency range, respectively. Hence, consideration of diffusion will not alter the conclusions drawn on the shapes of Faradaic impedance.

VII. SIMPLIFICATION OF THE EXTENDED MODEL BASED ON THE RATE-DETERMINING TERM

Since we know from the above example that diffusion in the low-frequency range does not change the shape of impedance plot in the high-frequency range, diffusion will be neglected for the moment. The primary purpose of this section is to verify whether the correlation between impedance shape and catalytic activity observed in the single-adsorbate example is valid for more general cases. Since the generalized model is too complicated for further manipulation, we apply the concept of the rate-determining term (RDT) introduced recently for this purpose [54].

Let us consider a serial reaction pathway, simplified from the mechanism in Eq. (42):

$$
\begin{aligned}
R + {}^* + n_1 e &\leftrightarrow I_1, \\
I_1 + n_2 e &\leftrightarrow I_2, \\
&\cdots \\
I_{i-1} + n_i e &\leftrightarrow I_i, \\
&\cdots \\
I_N + n_{N+1} e &\leftrightarrow P + {}^*,
\end{aligned}
\tag{67}
$$

where * represents free sites, R is the reactant, P is the product, I_i $(i = 1, \ldots, N)$ are adsorbed intermediates, and n_i is the electron number. Solution species, e.g., hydronium ions, may participate in elementary steps. Since the diffusion of soluble species is to be neglected, their influences on the kinetics can be implicitly embedded into the rate constants, $k_i^{\pm}$ (+ forward reaction, − backward reaction).

In previous work [54], the overall rate of this reaction under steady states, denoted j_{ss}, was approximated as

$$
-\frac{ne\rho}{j_{ss}} \approx \sum_{i=1}^{N+1} \frac{\Theta_i}{k_i^+},
\tag{68}
$$

where $n = \sum_{i=1}^{N+1} n_i$ is the total number of electrons, ρ is the number density of active sites, and $Q = e\rho$.

Θ_i are thermodynamic factors given by

$$
\Theta_i = \frac{\sum_{j=0}^{N} \prod_{s=1}^{j} K_{\mathbf{P}(i,+s)}}{\prod_{s=1}^{N} K_{\mathbf{P}(i,+s)}},
\tag{69}
$$

where $K_i = k_i^+ / k_i^-$ is the equilibrium constant of the ith elementary step, $\mathbf{P}(i, \pm j)$ is the permutation operator introduced in Ref. [54]. Its calculation rules and examples of applying it can be found there.

The key point is that the overall reaction resistance, $-(ne\rho/j_{ss})$, is decomposed into $(N+1)$ resistance terms in Eq. (68). Each term has same mathematical structure, which is the ratio of a thermodynamic term composed of thermodynamic constants, K_i, to a single forward-reaction rate, k_i^+. As we have shown in previous work [54], one of the $(N+1)$ resistance terms is usually larger by several orders of magnitude than the rest. This term determining the overall reaction resistance is defined as the RDT.

Under the RDT approximation, we further simplify Eq. (68) to

$$
j_{ss} \approx -\frac{nQk_d^+}{\Theta_d},
\tag{70}
$$

where d denotes the serial number of the step corresponding to k_d^+ in the RDT.

If we neglect the relaxation dynamics of adsorption (desorption) of intermediates, we can define an effective charge-transfer resistance from j_{ss}:

$$
R_{ct}^{eff} \approx -\frac{\Theta_d^2}{nQ}\left(\frac{\partial k_d^+}{\partial E_M}\Theta_d - \frac{\partial \Theta_d}{\partial E_M}k_d^+\right)^{-1},
\tag{71}
$$

A parallel connection of R_{ct}^{eff} and the double-layer capacitance, C_{dl}, leads to a semicircle in the Nyquist plot. As stressed by Harrington recently, R_{ct}^{eff} is different from the charge-transfer resistance of the dth step [31].

When the relaxation dynamics of adsorbed intermediates are considered, more complex shapes of impedance plots may occur. Let us focus on the dth step. Upon linear perturbation, the variation in the net rate of this step is written as

$$
\tilde{v}_d = \tilde{k}_d^+ \bar{\theta}_{d-1} + \bar{k}_d^+ \tilde{\theta}_{d-1} - (\tilde{k}_d^- \bar{\theta}_d + \bar{k}_d^- \tilde{\theta}_d),
\tag{72}
$$

Since the steps before this step are in quasiequilibrium, $\tilde{\theta}_{d-1}$ is calculated as

$$\tilde{\theta}_{d-1} = \frac{\partial \bar{\theta}_{d-1}}{\partial E_M} \tilde{E}. \tag{73}$$

$\tilde{\theta}_d$ is correlated with $\tilde{v}_d$ via

$$j\omega\tilde{\theta}_d = \tilde{v}_d, \tag{74}$$

where we have assumed $\tilde{v}_{d+1} = 0$, according to the RDT approximation.

We can now express $\tilde{\theta}_d$ as a function of $\tilde{E}$, and then calculate the variation in the Faradaic current density as

$$\tilde{i}_{\text{ct}} = -n_d Q \tilde{v}_d = -\frac{j\omega n_d Q}{j\omega + \bar{k}_d^-}$$
$$\times \left(\frac{\partial \bar{k}_d^+}{\partial E_M} \bar{\theta}_{d-1} + \frac{\partial \bar{\theta}_{d-1}}{\partial E_M} \bar{k}_d^+ - \frac{\partial \bar{k}_d^-}{\partial E_M} \bar{\theta}_d \right) \tilde{E}. \tag{75}$$

Then, the total impedance is obtained as

$$Z = 1 / \left(j\omega C_{\text{dl}} - \frac{j\omega n_d Q}{j\omega + \bar{k}_d^-} \right.$$
$$\left. \times \left(\frac{\partial \bar{k}_d^+}{\partial E_M} \bar{\theta}_{d-1} + \frac{\partial \bar{\theta}_{d-1}}{\partial E_M} \bar{k}_d^+ - \frac{\partial \bar{k}_d^-}{\partial E_M} \bar{\theta}_d \right) \right), \tag{76}$$

which can be transformed into the form of Eq. (11), with $\Delta_\theta = -\bar{k}_d^-$:

$$\Sigma_E = n_d Q \left(\frac{\partial \bar{k}_d^+}{\partial E_M} \bar{\theta}_{d-1} + \frac{\partial \bar{\theta}_{d-1}}{\partial E_M} \bar{k}_d^+ - \frac{\partial \bar{k}_d^-}{\partial E_M} \bar{\theta}_d \right),$$

and $\Sigma_\theta \Delta_E = \Delta_\theta \Sigma_E$, or into the form of Eq. (12) with

$$C_{\text{eff}}(\omega) = C_{\text{dl}} + \frac{\Sigma_\theta \Delta_E}{\omega^2 + \Delta_\theta^2},$$

and

$$R_{\text{eff}}(\omega) = \left(\frac{-\Sigma_E \omega^2}{\omega^2 + \Delta_\theta^2} \right)^{-1}.$$

Since $\Delta_\theta < 0$ and $\Sigma_E < 0$, we know $C_{\text{eff}}(\omega) > 0$ and $R_{\text{eff}}(\omega) > 0$ at any ω. In addition, R_{eff} increases with decreasing ω. Therefore, the EIS plot possesses only one semicircle in the first quadrant, and no inductive loop can be expected. Harrington discussed the EIS of a similar serial mechanism based on the rate-determining step (RDS) assumption [55]; see a comparison between RDT and RDS in Ref. [54]. Consistent with the present analysis, the RDS assumption leads to a Faradaic impedance being an effective charge-transfer resistance in parallel

with a pseudocapacitance. The present analysis also supports Lasia's recent claim that "they (inductive loops) cannot appear at far negative overpotentials where the kinetics is treated as irreversible" [38].

The analysis based on the rate-determining term can be summarized in the following remark.

Remark 14. If an electrocatalytic reaction is limited by a single RDS, the EIS plot possesses only one semicircle in the first quadrant, and no inductive loop can be expected. It is noted that the resistance of the semicircle is an effective charge-transfer resistance, rather than the charge-transfer resistance of the RDS.

VIII. EXPERIMENTAL EVIDENCE AND COMPARISON WITH WORKS IN THE LITERATURE

Despite the great complexity of the parametric space of electrocatalytic reactions, a few general observations regarding the EIS shape can be made from the preceding analysis. First, diffusion in the electrolyte solution in a finite space manifests as a closed arc in the low-frequency range and does not change the EIS shape in the high-frequency range. Therefore, we are only concerned about diffusion-free EIS in the following. Second, EIS plots of a single-adsorbate reaction on low-activity catalysts, i.e., where the adsorbate is either very strongly or weakly bound, have only a single semicircle, and no inductive loop exists. In other words, EIS plots consisting of two semicircles are more likely to be observed on more active catalysts, i.e., where the binding energy of the adsorbate is close to or exactly at the optimal value. Third, when assumptions of the rate-determining term or the rate-determining step are valid, the EIS plots show only one semicircle in the first quadrant, and no inductive loop can be expected. The third point is not limited to the single-adsorbate reaction, but general for any reactions. Fourth, an inductive loop is rare for electrocatalytic reactions on a stable catalyst without structural reconstruction or side reactions. It is more likely to observe the inductive loop at more active catalysts in the low-overpotential region. However, we do not observe the inductive loop for catalysts sitting exactly on the volcano peak.

Though an abundance of EIS data of a wide range of electrochemical reactions exists in the literature, an attempt to corroborate above conclusions requires a careful selection of experimental data. Severely distorted loops, either inductive or capacitive, are frequently observed in metal deposition and dissolution reactions in the field of corrosion [36,37,46,53,56–60]. These distorted loops are reported to be generated from dynamic growth and aging of the active sites, and interference of parasitic reactions such as adsorption of the electrolyte anions; see the review

by Wiart and co-workers [58]. These complexities are not considered in the present work, and these experimental data are not discussed here.

The hydrogen evolution reaction (HER) on metal surfaces is probably the most suitable reaction to corroborate the present theoretical analysis. On one hand, it involves only one active adsorbate, namely, the overpotential-deposited hydrogen, which greatly simplifies the theoretical analysis. On the other hand, experimental EIS data on an array of metals over a wide spectrum of binding strength of adsorbed hydrogen have been reported [61–65].

In Fig. 14, EIS plots for the HER at four metals are shown. According to Trasatti's volcano plot in Fig. 14(a), Bi and Pb belong to low-activity catalysts that bind the adsorbate too weakly, while Pd and Pt belong to high-activity catalysts that bind the adsorbate neither too weakly nor strongly [8]. Consistent with the present theoretical analysis, cf. **Remark 5** in Figs. 5 and 9, Bi and Pb are reported to have EIS shapes of a single semicircle at all examined potentials [64]. The scattered points in the low-frequency range are probably due to bubble formation. On the contrary, EIS shapes of two semicircles are observed
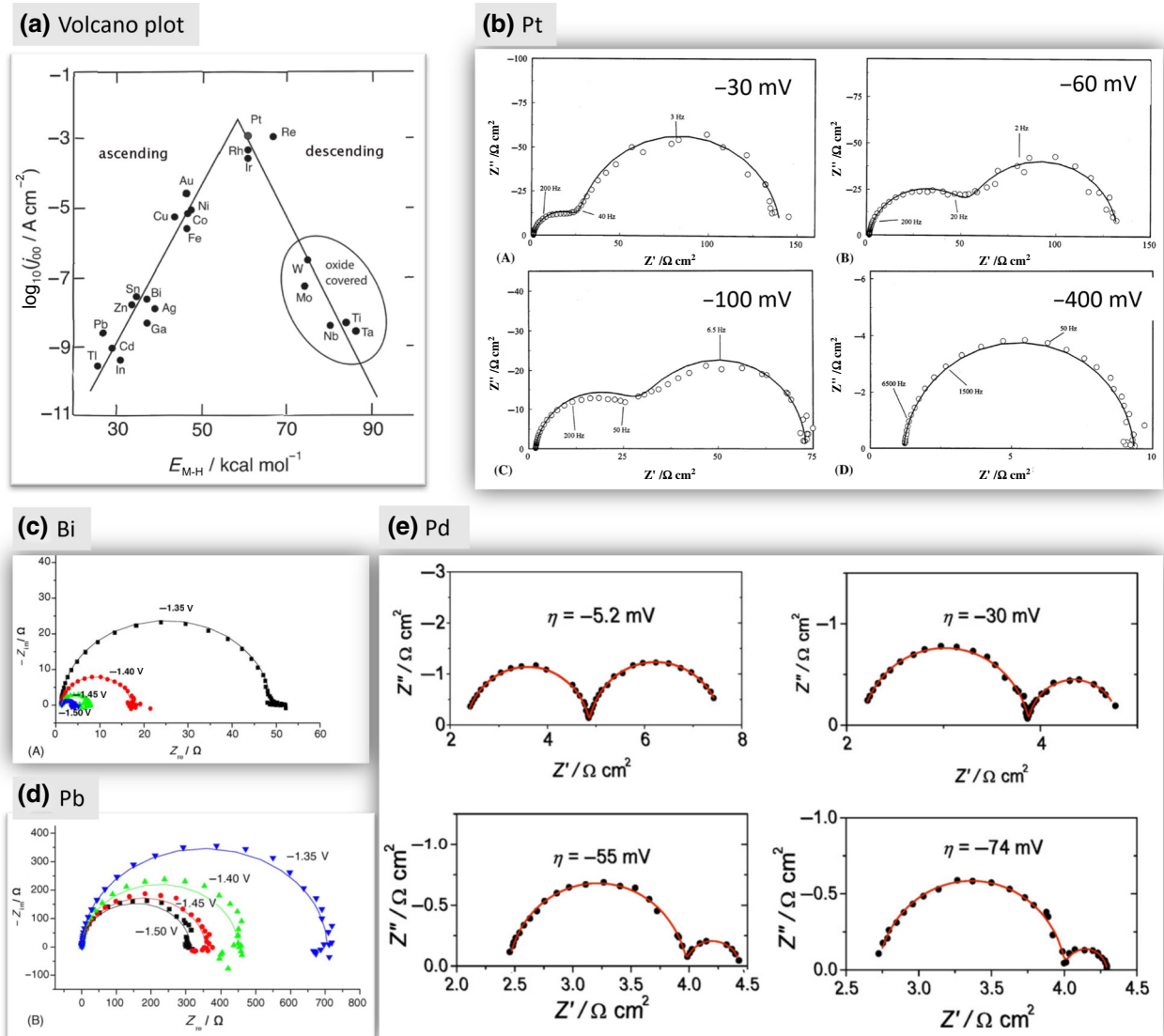

FIG. 14. Corroboration of theoretical analysis using experimental EIS data on hydrogen evolution reaction. (a) Trasatti's volcano plot for the hydrogen evolution reaction, reproduced with permission from Ref. [8]. (b) EIS plots of the hydrogen evolution reaction at Pt(100) in $0.5M$ NaOH at four overpotentials, reproduced with permission from Ref. [65]. Copyright (1999) Elsevier. EIS plots of the hydrogen evolution reaction on (c) Bi and (d) Pb electrodes in $4.79M$ H_2SO_4 solution at different potentials referenced to $Hg|Hg_2SO_4|1.28$ $g\,cm^{-3}$ H_2SO_4, reproduced with permission from Ref. [64] Copyright (2005) Elsevier. (e) EIS plots of the hydrogen evolution reaction on Pd in $0.1M$ H_2SO_4 at different potentials referenced to a reversible hydrogen electrode, reproduced with permission from Ref. [63] Copyright (2017) Elsevier.

for high-activity catalysts Pt [65] and Pd [63]. More interestingly, EIS shapes at Pt transit from two semicircles to one semicircle as the overpotential grows, as predicted in the present theoretical analysis, cf. **Remark 4** in Fig. 5 and **Remark 9** in Fig. 9. Two semicircles are also observed for the HER at other active catalysts like Rh [66] and Ru [67].

Last, but not least, no inductive loop is observed for the hydrogen evolution reaction, which also corroborates the claim that it is rare to observe an inductive loop for electrocatalytic reactions occurring on stable electrodes in clean and nonspecifically adsorbing electrolyte solutions. Nevertheless, absence of evidence is by no means evidence of absence. Angelo and Lasia observed an inductive loop at several overpotentials for hydrogen evolution on Ni-Zn alloy electrodes in alkaline solution [68]. Interestingly enough, Chen and Lasia did not observe the inductive loop for hydrogen evolution on Ni-Ali alloy electrodes in alkaline solution [69]. Furthermore, Angelo and Lasia reported that the model parameters fitted from the inductive loop were inconsistent with the usual Volmer-Heyrovsky-Tafel mechanism. A possible origin of the inductive loop is dissolution of Zn remained after the leaching process.

IX. CONCLUSION

Driven by the desire to search for possible correlations between EIS shapes and electrocatalytic activities, we started with the simplest case with a single adsorbate, for which we were allowed to draw a complete regime diagram of all possible EIS shapes, further, to prove and then, for more complicated cases, disprove several remarks on the EIS shapes. The EIS shapes are very sensitive to transfer coefficients and lateral interactions. We then generalized the impedance model for any electrocatalytic reactions considering mass transport in the electrolyte solution, demystified it using a simple example, and simplified it based on the rate-determining term assumption. Several pieces of conclusion survived the test of realistic complexities and were then subject to experimental testing using literature data on the hydrogen evolution reaction.

First, as far as diffusion-free EIS is concerned, unless otherwise noted, the use of assumptions of the rate-determining term or the rate-determining step leads to EIS plots of only one semicircle in the first quadrant, and no inductive loop exists. In other words, observations of two or more semicircles indicate that more than one step determines the reaction rate, if there is no side reaction or structural instabilities. Second, for single-adsorbate reactions, low-activity catalysts, i.e., those binding the intermediate either too strongly or weakly, exhibit only a single semicircle. Examples are Bi and Pb for hydrogen evolution reactions. In other words, EIS plots consisting of two semicircles are more likely to be observed on highly active catalysts, i.e., where the binding energy of the adsorbate is close to the optimal value. Examples include Pt and Pd

for hydrogen evolution reactions. Third, an inductive loop is rare for electrocatalytic reactions on stable electrodes in clean and nonspecifically-adsorbing electrolyte solutions, namely, without dynamic evolution of active sites or side reactions. Fourth, for single-adsorbate reactions, the feasible region for an inductive loop is narrowed to highly active catalysts in the low-overpotential region. It should be noted that the present simulations do not address frequency dispersion, coexisting competing reactions, or the influence of nonuniform current and potential distributions that can confound experimental results.

[1] B. Hammer and J. K. Nørskov, in *Advances in Catalysis*, edited by B. C. Gates and H. Knozinger (Academic Press, New York, 2000), Vol. 45, pp. 71–129.

[2] J. K. Nørskov, T. Bligaard, J. Rossmeisl, and C. H. Christensen, Towards the computational design of solid catalysts, Nat. Chem. **1**, 37 (2009).

[3] Z. W. Seh, J. Kibsgaard, C. F. Dickens, I. Chorkendorff, J. K. Nørskov, and T. F. Jaramillo, Combining theory and experiment in electrocatalysis: Insights into materials design, Science **355**, eaad4998 (2017).

[4] B. Hammer and J. K. Nørskov, Electronic factors determining the reactivity of metal surfaces, Surf. Sci. **343**, 211 (1995).

[5] A. Kulkarni, S. Siahrostami, A. Patel, and J. K. Nørskov, Understanding catalytic activity trends in the oxygen reduction reaction, Chem. Rev. **118**, 2302 (2018).

[6] S. Divanis, T. Kutlusoy, I. M. Ingmer Boye, I. C. Man, and J. Rossmeisl, Oxygen evolution reaction: A perspective on a decade of atomic scale simulations, Chem. Sci. **11**, 2943 (2020).

[7] J. K. Nørskov, T. Bligaard, A. Logadottir, J. R. Kitchin, J. G. Chen, S. Pandelov, and U. Stimming, Trends in the exchange current for hydrogen evolution, J. Electrochem. Soc. **152**, J23 (2005).

[8] P. Quaino, F. Juarez, E. Santos, and W. Schmickler, Volcano plots in hydrogen electrocatalysis – uses and abuses, Beilstein J. Nanotechnol. **5**, 846 (2014).

[9] B. Ershler, Investigation of electrode reactions by the method of charging-curves and with the aid of alternating currents, Discuss. Faraday Soc. **1**, 269 (1947).

[10] J. E. B. Randles, Kinetics of rapid electrode reactions, Discuss. Faraday Soc. **1**, 11 (1947).

[11] H. Gerischer and W. Mehl, Zum Mechanismus der kathodischen Wasserstoffabscheidung an Quecksilber, Silber und Kupfer, Zeitschrift für Elektrochemie **59**, 1049 (1955).

[12] I. Epelboin and M. Keddam, Faradaic impedances: Diffusion impedance and reaction impedance, J. Electrochem. Soc. **117**, 1052 (1970).

[13] R. D. Armstrong and M. Henderson, Impedance plane display of a reaction with an adsorbed intermediate, J. Electroanal. Chem. Interfacial Electrochem. **39**, 81 (1972).

[14] S. Iseki, K. Ohashi, and S. Nagaura, Impedance of the oxygen-evolution reaction on noble metal electrodes, Electrochim. Acta **17**, 2249 (1972).

[15] J. P. Diard, B. Le Gorrec, and C. Montella, Impedance zone diagram of an oxidation mechanism in an adsorbed phase with chemical recombination, J. Electroanal. Chem. Interfacial Electrochem. **161**, 235 (1984).

[16] D. A. Harrington and B. E. Conway, ac impedance of Faradaic reactions involving electrosorbed intermediates—I. Kinetic theory, Electrochim. Acta **32**, 1703 (1987).

[17] J. P. Diard, P. Landaud, B. Le Gorrec, and C. Montella, Calculation, simulation and interpretation of electrochemical impedance: Part II. Interpretation of Volmer-Heyrovsky impedance diagrams, J. Electroanal. Chem. Interfacial Electrochem. **255**, 1 (1988).

[18] C.-n. Cao, On the impedance plane displays for irreversible electrode reactions based on the stability conditions of the steady-state—I. One state variable besides electrode potential, Electrochim. Acta **35**, 831 (1990).

[19] J. P. Diard, B. Le Gorrec, and C. Montella, Calculation, simulation and interpretation of electrochemical impedances: Part 3. Conditions for observation of low frequency inductive diagrams for a two-step electron transfer reaction with an adsorbed intermediate species, J. Electroanal. Chem. **326**, 13 (1992).

[20] D. A. Harrington, Electrochemical impedance of multistep mechanisms: Mechanisms with diffusing species, J. Electroanal. Chem. **403**, 11 (1996).

[21] D. A. Harrington, Electrochemical impedance of multistep mechanisms: A general theory, J. Electroanal. Chem. **449**, 9 (1998).

[22] D. A. Harrington, Electrochemical impedance of multistep mechanisms: Mechanisms with static species, J. Electroanal. Chem. **449**, 29 (1998).

[23] D. A. Harrington and P. van den Driessche, Impedance of multistep mechanisms: Equivalent circuits at equilibrium, Electrochim. Acta **44**, 4321 (1999).

[24] D. A. Harrington and P. van den Driessche, Stability and electrochemical impedance of mechanisms with a single adsorbed species, J. Electroanal. Chem. **501**, 222 (2001).

[25] T. Pajkossy and D. M. Kolb, Double layer capacitance of Pt(111) single crystal electrodes, Electrochim. Acta **46**, 3063 (2001).

[26] A. Lasia, in *Modern Aspects of Electrochemistry*, edited by B. E. Conway, J. O'M Bockris, and R. E. White (Springer, New York, 1999), Vol. 32, pp.143–248.

[27] J. Sengoku, M. Naito, H. Okamoto, T. Ogita, and S. Ichikawa, On the visibility of fast reactions in electrochemical impedance spectroscopy, Chem. Phys. Lett. **525–526**, 125 (2012).

[28] V. I. Kichigin and A. B. Shein, Diagnostic criteria for hydrogen evolution mechanisms in electrochemical impedance spectroscopy, Electrochim. Acta **138**, 325 (2014).

[29] D. A. Harrington, The rate-determining step in electrochemical impedance spectroscopy, J. Electroanal. Chem. **737**, 30 (2015).

[30] V. I. Kichigin and A. B. Shein, Influence of hydrogen absorption on the potential dependence of the Faradaic impedance parameters of hydrogen evolution reaction, Electrochim. Acta **201**, 233 (2016).

[31] D. A. Harrington, Simplifying mechanistic impedances, Electrochim. Acta **338**, 135895 (2020).

[32] J. Huang, Electrochemical impedance spectroscopy for electrocatalytic interfaces and reactions: Classics never die, J. Electrochem. **26**, 3 (2020).

[33] P. Dolin and B. Ershler, The kinetics of discharge and ionization of hydrogen adsorbed at Pt-electrode, Acta Physicochim. URSS **13**, 747 (1940).

[34] M. B. Molina Concha, M. Chatenet, C. Montella, and J. P. Diard, A Faradaic impedance study of E-EAR reaction, J. Electroanal. Chem. **696**, 24 (2013).

[35] J. P. Diard and C. Montella, Non-intuitive features of equivalent circuits for analysis of EIS data. The example of EE reaction, J. Electroanal. Chem. **735**, 99 (2014).

[36] C. Gabrielli, Identification of Electrochemical Processes by Frequency Response Analysis, *Technical Report Number 04/83*, **2**, 25 (1984).

[37] A. Lasia, in *Modern Aspects of Electrochemistry*, edited by Conway B. E., White R. E. (Springer US, Boston, MA, 2002), Vol. 35, pp. 1–49.

[38] A. Lasia, Mechanism and kinetics of the hydrogen evolution reaction, Int. J. Hydrogen Energy **44**, 19484 (2019).

[39] B. Łosiewicz, R. Jurczakowski, and A. Lasia, Kinetics of hydrogen underpotential deposition at iridium in sulfuric and perchloric acids, Electrochim. Acta **225**, 160 (2017).

[40] J. Bisquert, Negative inductor effects in nonlinear two-dimensional systems: Oscillatory neurons and memristors, Chem. Phys. Rev. **3**, 041305 (2022).

[41] J. Bisquert and A. Guerrero, Chemical inductor, J. Am. Chem. Soc. **144**, 5996 (2022).

[42] Y. Zhang, J. Huang, and M. Eikerling, Criterion for finding the optimal electrocatalyst at any overpotential, Electrochim. Acta **400**, 139413 (2021).

[43] See the Supplemental Material at http://link.aps.org/supplemental/10.1103/PRXEnergy.3.023001 for the PYTHON code used to generate the figures in this work.

[44] Y. Zhang, J. Zhang, and J. Huang, Potential-dependent volcano plot for oxygen reduction: Mathematical origin and implications for catalyst design, J. Phys. Chem. Lett. **10**, 7037 (2019).

[45] S. Razzaq and K. S. Exner, Materials screening by the descriptor $G_{max}(\eta)$: The free-energy span model in electrocatalysis, ACS Catal. **13**, 1740 (2023).

[46] N. M. Marković, T. J. Schmidt, B. N. Grgur, H. A. Gasteiger, R. J. Behm, and P. N. Ross, Effect of temperature on surface processes at the Pt(111)−liquid interface: Hydrogen adsorption, oxide formation, and CO oxidation, J. Phys. Chem. B **103**, 8568 (1999).

[47] R. Gómez, J. M. Orts, B. Álvarez-Ruiz, and J. M. Feliu, Effect of temperature on hydrogen adsorption on Pt(111), Pt(110), and Pt(100) electrodes in 0.1M HClO₄, J. Phys. Chem. B **108**, 228 (2004).

[48] L. E. Botello, J. M. Feliu, and V. Climent, Activation energy of hydrogen adsorption on Pt(111) in alkaline media: An impedance spectroscopy study at variable temperatures, ACS Appl. Mater. Interfaces **12**, 42911 (2020).

[49] V. Climent, R. Gómez, J. M. Orts, and J. M. Feliu, Thermodynamic analysis of the temperature dependence of OH adsorption on Pt(111) and Pt(100) electrodes in acidic media in the absence of specific anion adsorption, J. Phys. Chem. B **110**, 11344 (2006).

[50] E. Herrero and J. M. Feliu, Understanding formic acid oxidation mechanism on platinum single crystal electrodes, Curr. Opin. Electrochem. **9**, 145 (2018).

[51] X. Zhu, J. Huang, and M. Eikerling, pH effects in a model electrocatalytic reaction disentangled, JACS Au **3**, 1052 (2023).

[52] M.-K. Zhang, Z. Wei, W. Chen, M.-L. Xu, J. Cai, and Y.-X. Chen, Bell shape vs volcano shape pH dependent kinetics of the electrochemical oxidation of formic acid and formate, intrinsic kinetics or local pH shift?, Electrochim. Acta **363**, 137160 (2020).

[53] J. Barber, S. Morin, and B. E. Conway, Specificity of the kinetics of H_2 evolution to the structure of single-crystal Pt surfaces, and the relation between opd and upd H, J. Electroanal. Chem. **446**, 125 (1998).

[54] J. Huang, X. Zhu, and M. Eikerling, The rate-determining term of electrocatalytic reactions with first-order kinetics, Electrochim. Acta **393**, 139019 (2021).

[55] D. A. Harrington and P. van den Driessche, Mechanism and equivalent circuits in electrochemical impedance spectroscopy, Electrochim. Acta **56**, 8005 (2011).

[56] I. Epelboin and R. Wiart, Mechanism of the electrocrystallization of nickel and cobalt in acidic solution, J. Electrochem. Soc. **118**, 1577 (1971).

[57] E. Chassaing, M. Joussellin, and R. Wiart, The kinetics of nickel electrodeposition: Inhibition by adsorbed hydrogen and anions, J. Electroanal. Chem. Interfacial Electrochem. **157**, 75 (1983).

[58] R. Wiart, Elementary steps of electrodeposition analysed by means of impedance spectroscopy, Electrochim. Acta **35**, 1587 (1990).

[59] C. Cachet, F. Ganne, S. Joiret, G. Maurin, J. Petitjean, V. Vivier, and R. Wiart, EIS investigation of zinc dissolution in aerated sulphate medium. Part II: Zinc coatings, Electrochim. Acta **47**, 3409 (2002).

[60] D. Giménez-Romero, J. J. García-Jareño, and F. Vicente, EQCM and EIS studies of $Zn_{aq}^{2+} + 2e \rightleftarrows Zn^0$ electrochemical reaction in moderated acid medium, J. Electroanal. Chem. **558**, 25 (2003).

[61] Y. Choquette, L. Brossard, A. Lasia, and H. Menard, Study of the kinetics of hydrogen evolution reaction on Raney nickel composite-coated electrode by ac impedance technique, J. Electrochem. Soc. **137**, 1723 (1990).

[62] B. V. Tilak and C. P. Chen, Generalized analytical expressions for Tafel slope, reaction order and a.c. impedance for the hydrogen evolution reaction (HER): Mechanism of HER on platinum in alkaline media, J. Appl. Electrochem. **23**, 631 (1993).

[63] D. Lin and A. Lasia, Electrochemical impedance study of the kinetics of hydrogen evolution at a rough palladium electrode in acidic solution, J. Electroanal. Chem. **785**, 190 (2017).

[64] Y. M. Wu, W. S. Li, X. M. Long, F. H. Wu, H. Y. Chen, J. H. Yan, and C. R. Zhang, Effect of bismuth on hydrogen evolution reaction on lead in sulfuric acid solution, J. Power Sources **144**, 338 (2005).

[65] J. H. Barber and B. E. Conway, Structural specificity of the kinetics of the hydrogen evolution reaction on the low-index surfaces of Pt single-crystal electrodes in $0.5M$ dm^{-3} NaOH, J. Electroanal. Chem. **461**, 80 (1999).

[66] P. Wrona and A. Lasia, Experimental capacity of the rhodium electrode in $1M$ KOH and $0.5M$ H_2SO_4 solutions, Pol. J. Chem. **67**, 485 (1993).

[67] B. M. Jović, V. D. Jović, UČ Lačnjevac, S. I. Stevanović, J. Kovač, M. Radović, and N. V. Krstajić, Ru layers electrodeposited onto highly stable Ti_2AlC substrates as cathodes for hydrogen evolution in sulfuric acid solutions, J. Electroanal. Chem. **766**, 78 (2016).

[68] A. C. D. Angelo and A. Lasia, Surface effects in the hydrogen evolution reaction on Ni-Zn alloy electrodes in alkaline solutions, J. Electrochem. Soc. **142**, 3313 (1995).

[69] L. Chen and A. Lasia, Study of the kinetics of hydrogen evolution reaction on nickel-zinc alloy electrodes, J. Electrochem. Soc. **138**, 3321 (1991).